iScience

CellPress

Article

# Surface Stabilization of O3-type Layered Oxide Cathode to Protect the Anode of Sodium Ion Batteries for Superior Lifespan

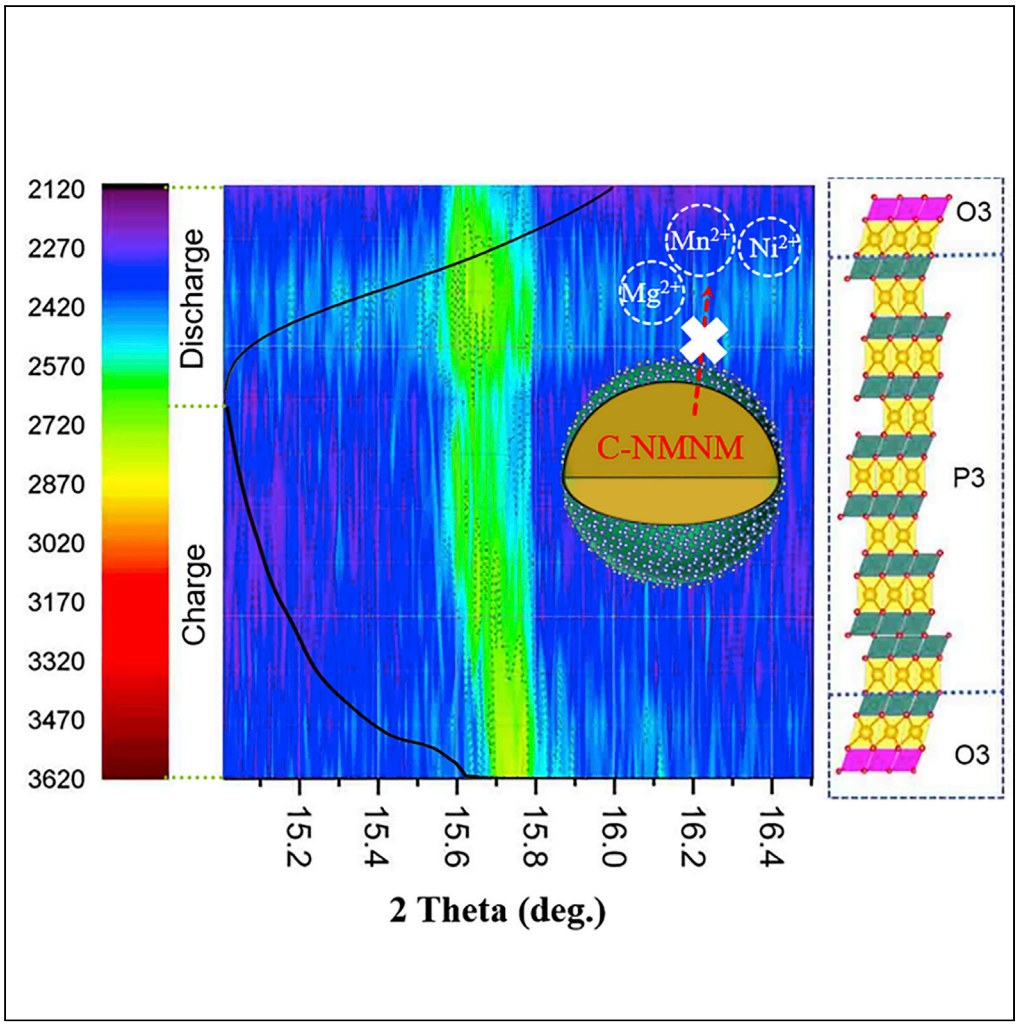


Qi Zhang, Qin-Fen Gu, Yang Li, Hai-Ning Fan, Wen-Bin Luo, Hua- Kun Liu, Shi-Xue Dou

qinfeng@ansto.gov.au (Q.-F.G.)
luow@uow.edu.au (W.-B.L.)

## HIGHLIGHTS

A thin layer of $AlPO_4$ can improve the cathode environmental stability

The thin layer can stabilize the cathode surface crystal structure

The thin layer can suppress DMD process to keep the anode resistance stable

The obtained material shows 95% capacity retention after cycling in a half-cell

Zhang et al., iScience *19*, 244–254
September 27, 2019 
https://doi.org/10.1016/j.isci.2019.07.029

iScience

CellPress

Article

# Surface Stabilization of O3-type Layered Oxide Cathode to Protect the Anode of Sodium Ion Batteries for Superior Lifespan

Qi Zhang,[1] Qin-Fen Gu,[2,*] Yang Li,[1] Hai-Ning Fan,[1] Wen-Bin Luo,[1,3,*] Hua- Kun Liu,[1] and Shi-Xue Dou[1]

## SUMMARY

**Even though the energy density of O3-type layer-structured metal oxide cathode can fully reach the requirement for large-scale energy storage systems, the cycling lifespan still cannot meet the demand for practical application once it is coupled with a non-sodium-metal anode in full-cell system. Transition metal dissolution into the electrolyte occurs along with continuous phase transformation and accelerates deterioration of the crystal structure, followed by migration and finally deposition on the anode to form a vicious circle. Surface engineering techniques are employed to modify the interface between active materials and the electrolyte by coating them with a thin layer of $AlPO_4$ ion conductor. This stable thin layer can stabilize the surface crystal structure of the cathode material by avoiding element dissolution. Meanwhile, it can protect the anode from increased resistance by suppressing the dissolution-migration-deposition process. This technique is a promising method to improve the lifetime for the future commercialization.**

## INTRODUCTION

Sodium ion batteries (SIBs) have been considered as one of the most promising systems to substitute for lithium ion batteries (LIBs) due to the increasing requirement for large-scale energy storage systems, the high abundance, and the economic efficiency of resources. During long-term academic research, industrial SIB prototypes have been created for practical application based on achievements on active materials development and similar fabrication techniques directly transferred from mature LIBs. Compared with the LIB system, however, the energy density and cycling lifetime of SIB system cannot simultaneously satisfy the basic requirements of the market for energy storage systems (Han et al., 2015; Lao et al., 2017; Deng et al., 2018a; Lu et al., 2018a, 2018b). Among the various promising cathode materials, O3-type layer-structured transition metal oxides (TMOs) have achieved huge success because they exhibit competitive performance and a comparable energy density to LIBs via composite and structure optimization. They have the advantage of high energy density resulting from their high operating potential, along with high specific capacity and good compatibility with the anode because of their high initial coulombic efficiency. Their energy density can reach as high as 210 Wh $kg^{-1}$, which can fully meet the requirement for large-scale energy storage systems (Xiao et al., 2018; Guo et al., 2015a; Yao et al., 2017; Wang et al., 2017; Deng et al., 2018, 2019; Gao et al., 2018; Rong et al., 2018; Zhu et al., 2019). Meanwhile, the mature and industrially feasible techniques to manufacture O3-type layer-structured TMOs have accelerated the progress toward practical application. Taking our group's previous work, for example, Mg and Cu element substitution can optimize their environmental stability and alleviate the continuous phase transformation by decreasing the energy barriers of the multiple phase transformations during sodium deintercalation and intercalation processes, and the environmental stability and cycling lifetime have been improved (Deng et al., 2018a, 2018b). The acidic electrolyte ions attack the cathode, however, and the dissolution of the transition metal (TM) elements in the electrolyte leads to the collapse of the crystal structure and capacity fading. Moreover, the dissolved metal ions will contaminate the electrolyte and the solid-electrolyte interphase layer (SEI), which is further deposited on the anode side, to form a vicious circle (Cho et al., 2003; Zhan et al., 2013; Yan et al., 2016; Banerjee et al., 2017a; Guo et al., 2017; Lu et al., 2018a, 2018b; Zhan et al., 2018). All these comprehensive factors from every section of the battery system will gradually degrade the full-cell system so that it exhibits unsatisfactory performance. Therefore the urgent issue that needs to be solved is how to improve the cycling lifetime of O3-type layer-structured metal oxides, particularly in a full-cell system with non-sodium metal as anode, from the perspective of the whole system rather than from that of individual sections. Herein, surface engineering is employed to modify the interface between the active materials and the electrolyte, further increasing the cycling lifetime of the full-cell system by suppressing the dissolution-migration-deposition (DMD) process. Owing to the strong resistance to the reaction with the electrolyte from the high electronegativity of

[1]Institute for Superconducting and Electronic Materials, University of Wollongong, Wollongong, NSW 2522 Australia

[2]Australian Synchrotron (ANSTO), 800 Blackburn Road, Clayton, VIC 3168, Australia

[3]Lead Contact

*Correspondence: qinfeng@ansto.gov.au (Q.-F.G.), luow@uow.edu.au (W.-B.L.)

https://doi.org/10.1016/j.isci.2019.07.029

 

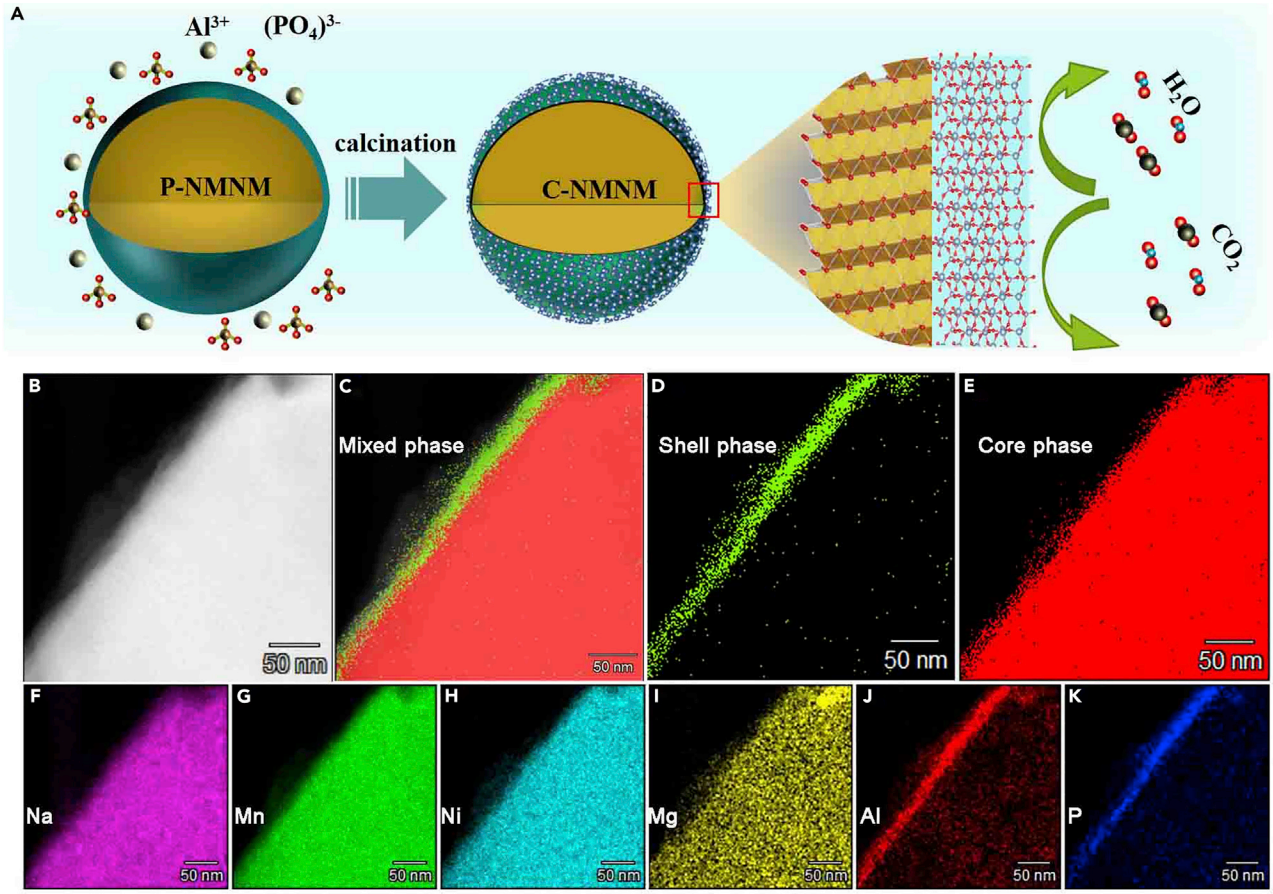


**Figure 1. Morphology and Phase of C-NMNM**

(A) Schematic illustration of the synthetic process for the $AlPO_4$ coating on the surface of $Na[Li_{0.05}Mn_{0.50}Ni_{0.30}Cu_{0.10}Mg_{0.05}]O_2$.

(B) High-angle annular dark field (HAADF)-STEM image.

STEM-EDS mapping of crystalline phase: Mixed phase of C-NMNM (C), $AlPO_4$ shell phase (D) and core phase of Na[Li0.05Mn0.50Ni0.30Cu0.10Mg0.05]O2 (E).

(F–K) Element Na (F), Mn (G), Ni (H), Mg (I), Al (J) and P (K) distributions from the edge to the bulk material of C-NMNM.

See also Figures S1–S5.

$(PO_4)^{3-}$ polyanions with $Al^{3+}$ cations, the surface modification by coating with a stable $AlPO_4$ protective thin layer in this work not only can alleviate the crystal structure collapse of the cathode material but also can protect the anode in the full-cell system by inhibiting the DMD process. Meanwhile, this thin protective layer can further improve its environmental stability in the ambient environment (Jung and Han, 2013; Yang et al., 2014; Kim et al., 2014; Park et al., 2015).

## RESULTS AND DISCUSSION

### Morphology and Structure Characterization of C-NMNM

The schematic diagram in Figure 1A shows the surface modification process on $Na[Li_{0.05}Mn_{0.50}Ni_{0.30}Cu_{0.10}Mg_{0.05}]O_2$ (P-NMNM) cathode material. A completely ionized solution consisting of aluminum ions and phosphate anions can be deposited uniformly on the surface of the cathode material particles by a rotary evaporator. Then, the residue is calcined at 400°C for 1 h, and the final air-stable $Na[Li_{0.05}Mn_{0.50}Ni_{0.30}Cu_{0.10}Mg_{0.05}]O_2$ coated with a thin layer of $AlPO_4$ (C-NMNM) was obtained. The obtained product has an X-ray diffraction (XRD) pattern that indicates the standard same XRD phase of O3-type layer-structured cathode material as the pure material and that $AlPO_4$ (indexed to 00-050-0054) was formed on the surface of the pure cathode material in Figure S1 in the Supplemental Information. The structure was investigated in further detail by scanning transmission electron microscopy (STEM) assisted by energy-dispersive spectroscopy (EDS), as shown in Figures 1B–1K and Figures S2 and S3. From the composite and phase

distribution, as shown in Figures 1C–1E, S2I, and S2J, it is clearly concluded that there are two phases in the composite with a core-shell structure. The entire bulk is uniformly wrapped by the protection layer. In the individual phase area, different elements, such as Na, Mn, Ni, and Mg, have a uniform distribution in the core phases. In the layer phase, Al and P exhibit a uniform distribution as well. All these results provide strong evidence to confirm that there is a thin layer of homogeneous coating.

To analyze the composite with the coating layer and the interface between the core materials and the coating layer, high-angle annular dark-field (HAADF)-STEM assisted by electron energy loss spectroscopy (EELS) was utilized at atomic resolution in Figure S4. In Figures S4A and S4B, the obtained C-NMNM retains the layered structure with an ~3-nm uniform coating layer, which was also confirmed by HAADF-STEM-EDS as shown in Figures S2 and S3. Owing to the unstable $AlPO_4$ under high voltage, the lattice pattern was not seen by STEM. In Figures S4C–S4E, it is seen that the particle of C-NMNM was well crystallized with lattice spacing of 2.56 and 2.44 Å, corresponding to the spacings of the (101) and (012) planes of bulk P-NMNM, which is consistent with the intensity profiles along the bright bands in Figure S4C. After surface modification, the bulk material shows no change, and the $Al^{3+}$ barely diffuses into the bulk material to form a different phase. The Al and P elements are precisely dispersed in the surface area, implying that $AlPO_4$ exists as a physically distinct phase attached to the P-NMNM surface, which is consistent with the result of Powder X-ray diffraction (PXRD) (Figure S1) and X-ray photoelectron spectroscopy (XPS) in Figure S5. To understand the core-shell interface of the C-NMNM deeply, EELS characterization and the corresponding spectra were simultaneously obtained on different selected areas of the C-NMNM particle, as shown in Figures S4F and S4G. In Figure S4F, Al-O and P-O bonds are detected in the edge area. After surface modification, the intensity of the Mn and Ni signals showed no obvious shift (Figure S4I), indicating that the coating layer of $AlPO_4$ has no effect on the crystal structure of the active material. All these characterizations demonstrate that this approach for modifying the P-NMNM surface yields a continuous surface region without disturbing the layered crystalline structure. These types of thin-layer coating are beneficial to the material stability as well (Cho et al., 2003; Xiao et al., 2013; Yang et al., 2014; Yan et al., 2016; Guo et al., 2017).

## Electrochemical Performance in Half- and Full-Cell Systems

The electrochemical performances of P-NMNM and C-NMNM were characterized for comparison within the voltage range of 2.0–4.0 V. To clarify the capacity contribution from the $AlPO_4$ in the composite for the cathode materials, the charge-discharge curves of the pure $AlPO_4$ were measured, and no plateau was observed in the voltage range of 2.0–4.0 V as shown in Figure S6, indicating that the reversible capacity is negligible in the voltage range of 2.0–4.0 V. The electrochemical performances of the P-NMNM and C-NMNM electrodes were measured at the 0.5 and 1 C rates within the potential range from 2.0 to 4.0 V versus Na/Na+, respectively. The charge and discharge profiles of these cathode materials have similar plateaus, as shown in Figure S7. C-NMNM delivers 138 mAh $g^{-1}$ at 0.5 C, whereas P-NMNM achieves 150 mAh $g^{-1}$. At the 1 C rate, these electrodes also show relatively high reversible capacity of 114 and 125 mAh $g^{-1}$, respectively (Figures 2A and 2B). These results show that surface modification will result in a slight capacity loss. To further study the long-term cycling performance (Figures 2C and 2D), the C-NMNM electrode was found to retain 87% and 95% of its capacity for 400 cycles at 0.5 C and 1 C, respectively, which was much more stable than P-NMNM (67% and 81%). This indicates that the C-NMNM electrode maintains better structural stability compared with the P-NMNM electrode (Alvarado et al., 2017). Meanwhile, the coulombic efficiency of C-NMNM over the whole cycling process is above 99.0%, which can meet the requirement for practical application. This significant improvement was mainly attributed to the $AlPO_4$ surface segregation, which, to some extent, protects the bulk materials from corrosion by the acidic electrolyte and structural collapse during the phase transformation. To evaluate the overall performance of C-NMNM, a comparison of stability has been made between C-NMNM and other published layered metal oxides in Figures 2E and 2F. During cycling at the 0.5 C (Figure 2E) and 1 C rates (Figure 2F), the capacity retention of C-NMNM is superior to those of the different kinds of P2, O3, and P2/O3-type cathode materials (Yao et al., 2017; Chen et al., 2015; Li et al., 2017; Guo et al., 2015a; Zhang et al., 2016a; Dai et al., 2017; Guo et al., 2017; Yao et al., 2017; Palanisamy et al., 2017; Wang et al., 2017; Gao et al., 2018; Hwang et al., 2018; Risthaus et al., 2018). It is concluded that the cycling lifespan can be dramatically optimized after surface modification.

To demonstrate the effects of the surface modification in a practical SIB, the full-cell system was assembled by coupling C-NMNM as the cathode material and hard carbon as the anode material (Figure S8). The detailed experimental information is similar to our previous work (Jianqiu, Wen-Bin et al. 2018). As shown in Figure 3A, the full-cell system was activated and operated at 0.1 C in the voltage window of 1.01–4.19 V. It had a high reversible efficiency, up to 70.6%, which means that there is an enormous store of cyclable

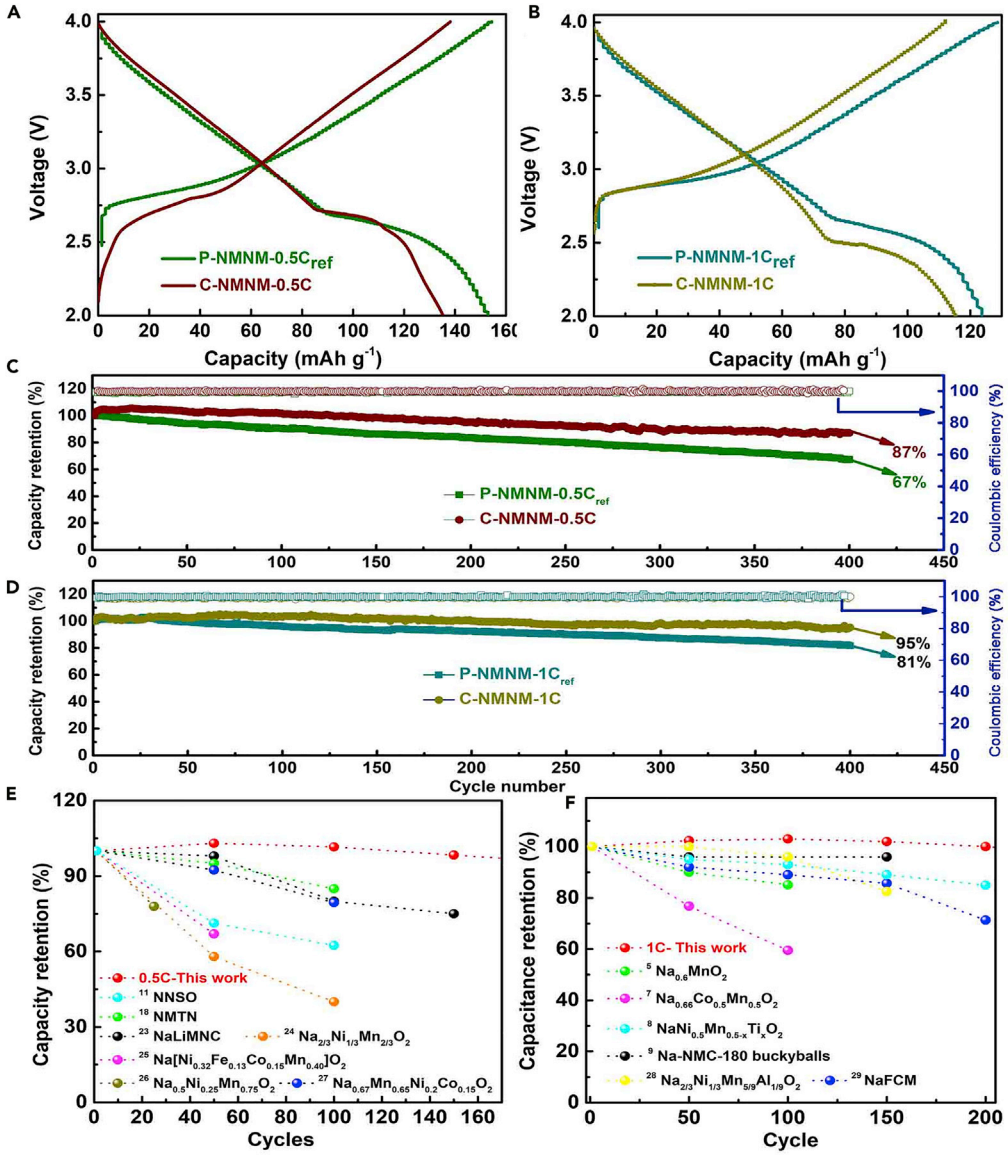


**Figure 2. Electrochemical Performance of the P-NMNM and C-NMNM Electrodes**

(A and B) The charge/discharge profiles (A) at the 0.5 C rate and (B) at the 1 C rate.

(C and D) Long-term cycle life and coulombic efficiency for 400 cycles at 0.5 C (C) and 1 C (D).

(E and F) Comparison of the capacity retention of C-NMNM electrodes against other cathode materials (E) at the 0.5 C rate11, 18, 23-27, and (F) at the 1 C rate5, 7-9 28, 29.

See also Figures S6 and S7.

sodium ions in the full-cell system after SEI formation on the anode. The full cells exhibited good cycling performance at 1 C over 200 cycles and had coulombic efficiency beyond 99% (Figure 3C). Moreover, the energy density of the full cell was as high as 210 Wh $kg^{-1}$, calculated on the basis of the total cathode and anode mass, which was roughly consistent with the result for a P-NMNM//hard carbon system (Figure 3B) (Guo et al., 2015a, 2015b; Li et al., 2015; Ren et al., 2016; Zhang et al., 2016b; Aragón et al., 2017; Yin et al., 2017; Yuan et al., 2017; Deng et al., 2018a, 2018b; Liu et al., 2018). To further investigate the kinetics of the electrode materials, the apparent activation energies (Figure 3D) of the two electrodes were calculated from the electrochemical impedance spectra, as shown in Figure S9 (Luo et al., 2014), which shows the Nyquist curves of the electrodes at a cathodic potential of 2.55 V versus $Na/Na^+$. Figure 3E shows the Arrhenius plots of log i0 as a function of $1{,}000T^{-1}$. The reaction associated with 2.55 V is mainly

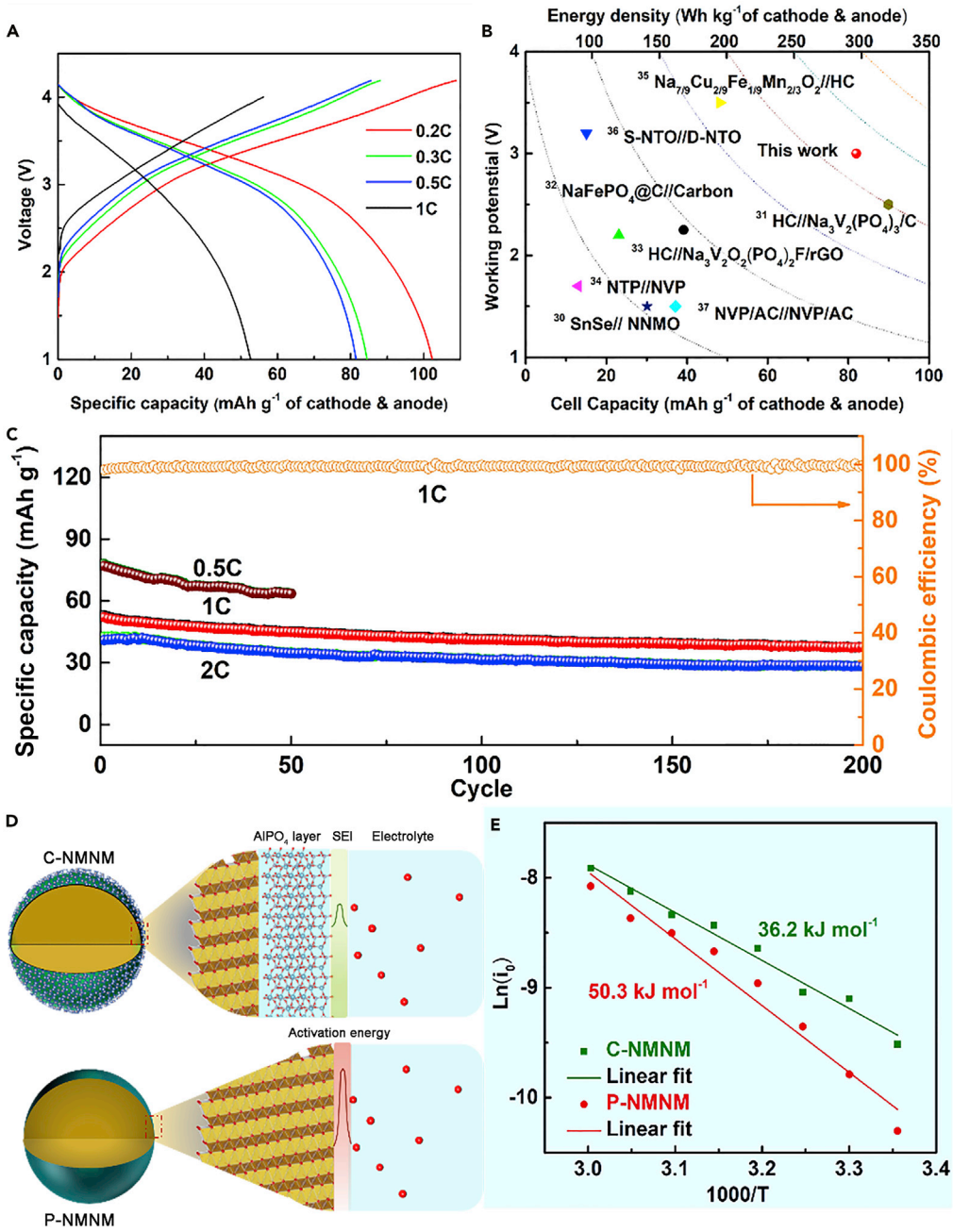


**Figure 3. Electrochemical Performance in Full-Cell and Activation Energy after Surface Modification**

(A) Charge and discharge curves for the full cell at different current densities.

(B) Comparison of the energy density of our full cell with reported sodium-ion full-cell systems.

(C) Cycling performance at 0.5 C of the full-cell system coupling C-NMNM as the cathode material and pristine hard carbon as the anode material.

(D) Schematic illustration of the activation energy of sodium ion transfer before and after the $AlPO_4$ coating was applied on the P-NMNM.

(E) Arrhenius plots showing the activation energy of the first discharge processes at a cathodic potential of 2.55 V versus Na/Na+.

See also Figures S8 and S9.

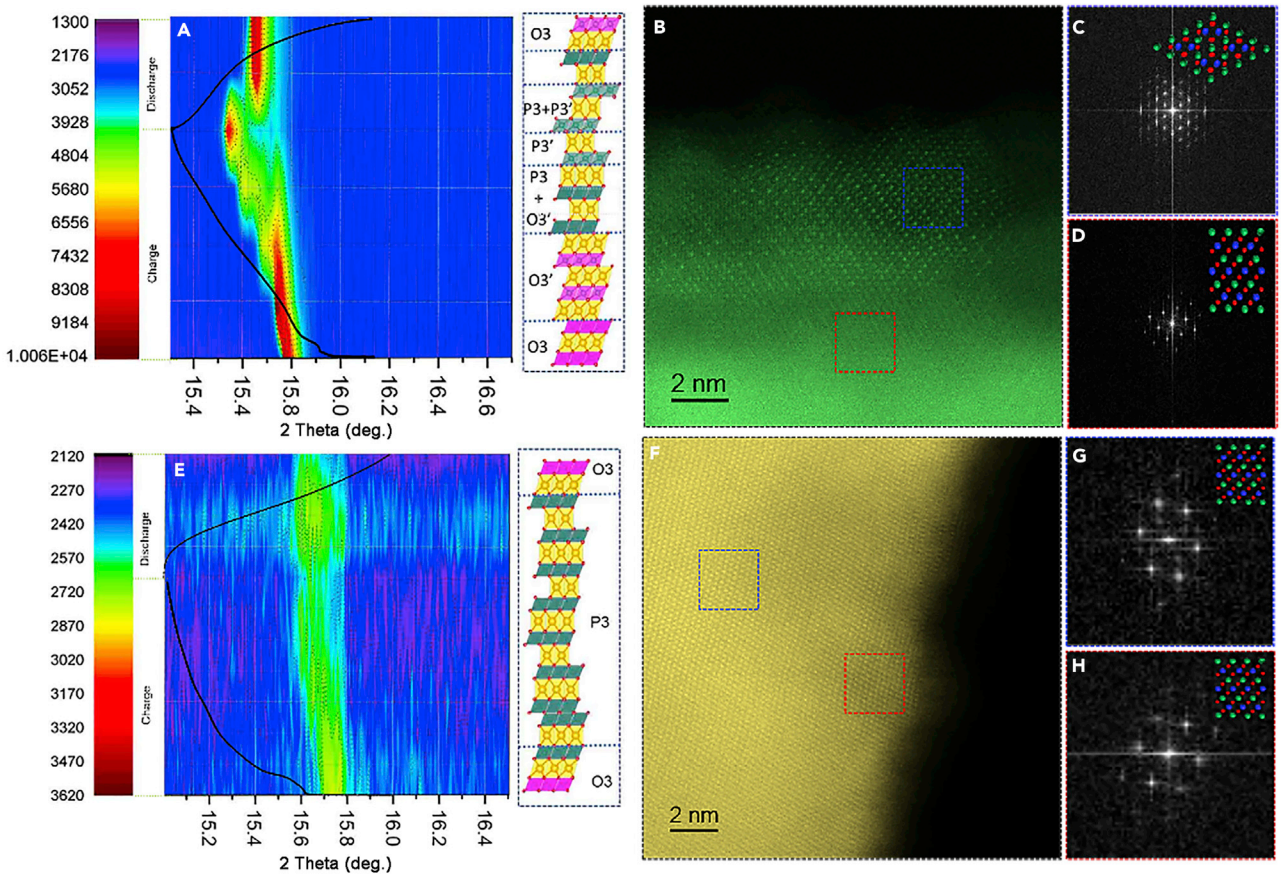


**Figure 4. The Structure Evolution of P-NMNM and C-NMNM after Long-Term Cycle**

(A) *In situ* synchrotron XRD patterns of P-NMNM during the 201st cycle.

(B) The detailed HAADF-STEM image of P-NMNM particle after 200 cycles (C) The corresponding Fast Fourier transform (FFT) of the edge area of the particle (the blue box in B). (D) The corresponding Fast Fourier transform (FFT) of the bulk area of the particle (the red box in B).

(E) *In situ* synchrotron XRD patterns of C-NMNM during the 201st cycle.

(F) The detailed HAADF-STEM image of C-NMNM particle after 200 cycles. (G) The corresponding Fast Fourier transform (FFT) of the edge area of the particle (the red box in F). (H) The corresponding Fast Fourier transform (FFT) of the bulk area of the particle (the grey box in F).

See also Figures S10 and S11.

contributed by the sodium ion insertion process into the cathode component. The activation energies ($E_a$ = -RK ln 10, where K = the slope of the fitting line) in Figure 3E of P-NMNM and C-NMNM were calculated to be 50.4 and 36.2 kJ $mol^{-1}$, respectively. Therefore, the excellent performance of C-NMNM, especially the cycling performance, can be mainly attributed to the lower ion apparent activation energy. In particular, the surface modification was designed to avoid destroying the crystal structure that gives rise to high ionic conductivity.

## Mechanism of Enhanced Stability of the C-NMNM

To monitor the phase transformation and interface in detail, *in situ* synchrotron technique and HAADF-STEM were employed on the materials after 200 cycles in the full-cell system as shown in Figure 4 and S10. In the case of P-NMNM, there is an obvious phase transformation between different structures, and some TM ions near the surface of the particle migrate into the Na layer, forming a spinel phase with Na+ occupying the tetrahedral sites, as shown in Figures 4A, 4B, and S11. The corresponding fast Fourier transform (FFT) results further confirm the change from the bulk (red) to the edge (blue) area with different lattice fringes and electronic diffraction spots, as shown in Figures 4B–4D. The sodium and other TM ordering is mainly preserved in the P-NMNM bulk after long cycling, whereas a fraction of cations migrate between the octahedral sites to the tetrahedral interstices in the surface. All the information obtained from C-NMNM, however, was completely different, as shown in Figures 4E–4H. The degree of phase

transformation from the *in situ* synchrotron results was decreased after surface modification, whereas the surface crystal structure of C-NMNM after 200 cycles could still maintain the layered structure, which is consistent with the pristine state. The corresponding FFT from the bulk (red) to the edge (blue) area in Figure 4F shows the same pattern. All the above comparative results indicate that thin-layer $AlPO_4$ surface modification can efficiently protect the surface crystal structure during long-term cycling to alleviate the degree of phase transformation. This improvement is beneficial for cycling lifespan enhancement as well.

To further explore the valence states, the electronic states for oxygen and TMs were collected by STEM-EELS at different positions from the bulk to the surface, as shown in the atomic-resolution STEM image in Figures 5A–5F. Each spectrum was averaged from an area with five rows of atomic columns to improve signal-to-noise ratios. In the case of P-NMNM, as shown in Figures 5A–5C, the pre-peak starts to decrease from the bulk to the surface. The content of O is lower in the surface than in the bulk, implying that oxygen vacancies have been formed within 5–10 nm of the surface. The reduced ratio of the O-K-edge pre-peak intensities to the main peak and the gradually decreased pre-peak indicates a change in the local oxygen environment, especially from the oxygen vacancies formed on the surface. It was claimed that oxygen was being released from the lattice and reacting with the electrolyte solvents through exothermic reactions (Qiao et al., 2015; Ma et al., 2017; Dai et al., 2018). In Figure 5B, the Mn L3 edge at the surface represents a lower energy loss compared with that of the bulk, which indicates a decrease in the oxidation state at the surface. Reduction of the transition-metal ions occurs together with migration of the transition-metal ions from the metal layer to the sodium interlayer through empty tetrahedral sites, thus causing a structural transformation from layered two-dimensional to spinel three-dimensional (Gao et al., 2019; Piao et al., 2019). A higher oxidation state in the bulk is also indicated by the higher O pre-peak intensity observed in the bulk, whereas the spinel oxidation state is indicated in the surface area. As shown in Figure 5D–5F, unlike the case of P-NMNM, it is observed that the reduced O pre-peak can be even seen at 15 nm for the C-NMNM sample, and there is no obvious change. The intensities of the O pre-peak and the main peak show no obvious change as well, implying that the active material is free from electrolyte corrosion and keeps its structure intact under the protection of the $AlPO_4$ (House et al., 2019; Kong et al., 2019). The Mn peak in the EELS spectrum of C-NMNM stays the same, showing that Mn ions are barely reduced during cycling. The intensity ratio of Mn L3/L2 in Figures 5C and 5F provides information on the Mn valence (oxidation) (Cho et al., 2015; Liu et al., 2015). The trends for cycled C-NMNM show that the oxidation state of Mn stays constant over the whole selected area, whereas the ratio for cycled P-NMNM is higher in the surface area. This indicates a lower oxidation state of Mn ($Mn^{3+}$ and $Mn^{2+}$) on the P-NMNM particle surface. These ions are easily dissolved in the electrolyte, leading to the collapse of the layered structure and the loss of active material. XPS was also used to examine surface changes at the cathode as a result of electrochemical cycling. Comparative studies of Mn 2p spectra before and after cycling confirm the Mn oxidation state in the surface of C-NMNM, as shown in Figure S12 (Zhan et al., 2013; Qiao et al., 2015; Banerjee et al., 2017b). To investigate the migration behavior of dissolved ions, scanning electron microscopy-EDS mapping of the hard carbon anode and the separator were conducted, as shown in Figure 5G, 5H, and S13, at a low magnification of 40 μm. In the case of the cell fabricated with C-NMNM, the Mn element was only slightly dissolved in the electrolyte, and there was no signal indicating deposition on the surface of the hard carbon anode, whereas there is a strong Mn signal on the hard carbon surface in the P-NMNM//hard carbon system. Meanwhile, the Mg element is also present in the electrolyte, which can be detected on the separator (Figure S14) (Xiao et al., 2013; Zhan et al., 2013; Piao et al., 2018; Zhan et al., 2018). All of this unexpected behavior will pollute the battery system. Taking the internal resistance as an example, as shown in Figure S15, on comparing with the results for C-NMNM, the charge transfer resistance ($R_{ct}$) of P-NMNM shows an increasing trend during cycling. Based on the above results, it is concluded that this surface engineering technique can efficiently stabilize the cathode surface to suppress the DMD process. Meanwhile, it can protect the whole battery system from unexpected contamination so as to increase the cycling lifespan.

In conclusion, the cathode TM elements near the surface dissolve, migrate, and are thus deposited on the hard carbon anode during long-term cycling. This not only can damage the surface crystal structure of the cathode material but also increases the cell resistance by contamination of the SEI layer during long-term cycling. In this work, surface engineering, by coating with a stable $AlPO_4$ thin layer, can efficiently suppress the DMD process by stabilizing the interface structure between the cathode and the electrolyte, particularly in a full-cell system. With the benefits of this surface protection engineering, the cathode can show 95% capacity retention after 400 cycles at 1 C. When coupled with hard carbon as anode, the full battery system can maintain 78% of the original value after 200 cycles at 1 C. This technique will lead to advanced

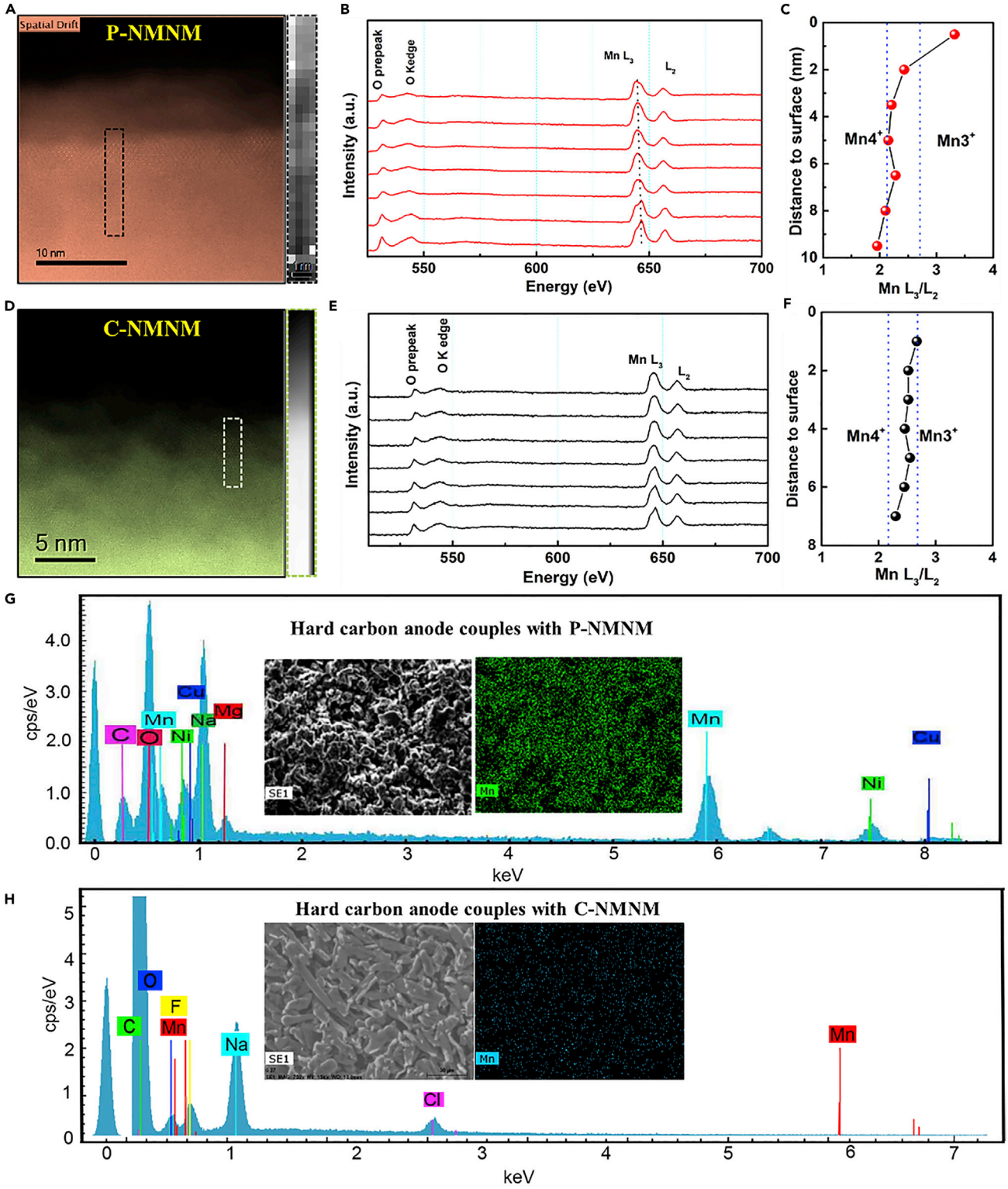


**Figure 5. Composition of Surface versus Bulk for P-NMNM (Top Row and G), and C-NMNM (Second Row from the Top and H)**

(A and D) STEM images of (A) P-NMNM and (D) C-NMNM.

Series of EELS spectra from the surface to the bulk of P-NMNM (B) and C-NMNM (E), corresponding to the HAADF images in (A) and (D).

**Figure 5. *Continued***
L3/L2 ratios corresponding to Mn of P-NMNM (C) and C-NMNM (F) , showing the decrease in oxidation state for Mn closer to the surface. The surface element distibution of Hard carbon anode coupled separately with P-NMNM (G) and C-NMNM (H).
See also Figures S12–S15.

SIBs that can meet the requirements for large-scale renewable energy storage, as well as inspire the development of a wide range of different electrode materials.

### Limitations of the Study

Although the coating layer can protect hard carbon anode, other types are not tested in this work, such as $MoS_2$. Meanwhile, the cathode material in this work should be air and water stable.

## METHODS

All methods can be found in the accompanying Transparent Methods supplemental file.

## SUPPLEMENTAL INFORMATION

Supplemental Information can be found online at https://doi.org/10.1016/j.isci.2019.07.029.

## ACKNOWLEDGMENTS

This work is supported by ARC-LIEF Grants (LE120100104 and LE0237478) and the China Scholarship Council (CSC). The authors would like to also thank Dr. Tania Silver for critical reading of the manuscript and also acknowledge the use of the facilities in the UOW Electron Microscopy Center, with particular thanks to Dr. Gilberto Casillas-Garcia. The manuscript was written through the contributions of all the authors. All authors have given approval to the final version of the manuscript. Part of experiment was conducted at PD beamline, Australian synchrotron (ANSTO).

## AUTHOR CONTRIBUTIONS

Methodology, Q.Z., Q.-F.G., and W.-B.L., Investigation, Q.Z., Y.L., H.-N.F., Q.-F.G, and W.-B.L.; Writing – Original Draft, Q.Z. and W.-B.L.; Writing – Review & Editing, Q.Z., Q.-F.G., and W.-B.L.; Funding Acquisition, S.-X.D.; Supervision, W.-B.L and S.-X.D.

## DECLARATION OF INTERESTS

The authors declare no competing interests.

Received: April 28, 2019
Revised: June 21, 2019
Accepted: July 18, 2019
Published: September 27, 2019

## REFERENCES

Alvarado, J., Ma, C., Wang, S., Nguyen, K., Kodur, M., and Meng, Y.S. (2017). Improvement of the cathode electrolyte interphase on P2-$Na_{2/3}Ni_{1/3}Mn_{2/3}O_2$ by atomic layer deposition. ACS Appl. Mater. Interfaces *9*, 26518–26530.

Aragón, M.J., Gutiérrez, J., Klee, R., Lavela, P., Alcántara, R., and Tirado, J.L. (2017). On the effect of carbon content for achieving a high performing Na3V2(PO4)3/C nanocomposite as cathode for sodium-ion batteries. J. Electroanal. Chem. *784*, 47–54.

Banerjee, A., Ziv, B., Shilina, Y., Luski, S., Aurbach, D., and Halalay, I.C. (2017a). Acid-scavenging separators: a novel route for improving li-ion batteries' durability. ACS Energy Lett. *2*, 2388–2393.

Banerjee, A., Shilina, Y., Ziv, B., Ziegelbauer, J.M., Luski, S., Aurbach, D., and Halalay, I.C. (2017b). On the oxidation state of manganese ions in Li-Ion battery electrolyte solutions. J. Am. Chem. Soc. *139*, 1738–1741.

Chen, X., Zhou, X., Hu, M., Liang, J., Wu, D., Wei, J., and Zhou, Z. (2015). Stable layered P3/P2 Na0.66Co0.5Mn0.5O2 cathode materials for sodium-ion batteries. J. Mater. Chem. A *3*, 20708–20714.

Cho, J., Kim, Y., Kim, B., Lee, J., and Park, B. (2003). A breakthrough in the safety of lithium secondary batteries by coating the cathode material with $AlPO_4$ nanoparticles. Angew. Chem. Int. Ed. *42*, 1618–1621.

Cho, H.M., Chen, M.V., MacRae, A.C., and Meng, Y.S. (2015). Effect of surface modification on nano-structured $LiNi_{0.5}Mn_{1.5}O_4$ spinel materials. ACS Appl. Mater. Interfaces *7*, 16231–16239.

Dai, H., Yang, C., Ou, X., Liang, X., Xue, H., Wang, W., and Xu, G. (2017). Unravelling the electrochemical properties and thermal behavior of $NaNi_{2/3}Sb_{1/3}O_2$ cathode for sodium-ion batteries by in situ X-ray diffraction investigation. Electrochim. Acta *257*, 146–154.

Dai, K., Wu, J., Zhuo, Z., Li, Q., Sallis, S., Mao, J., Ai, G., Sun, C., Li, Z., Gent, W.E., et al. (2018). High reversibility of lattice oxygen redox quantified by direct bulk probes of both anionic and cationic redox reactions. Joule *3*, 518–541.

Deng, J.Q., Luo, W.B., Chou, S.L., Liu, H.K., and Dou, S.X. (2018a). Sodium-ion batteries: from academic research to practical

commercialization. Adv. Energy Mater. *8*, 1701428.

Deng, J.Q., Luo, W.B., Xiao, L., Yao, Q.R., Wang, Z.M., Liu, H.K., Zhou, H.Y., and Dou, S.X. (2018b). High energy density sodium-ion battery with industrially feasible and air-stable O3-type layered oxide cathode. Adv. Energy Mater. *8*, 1701610.

Deng, Y.P., Wu, Z.G., Liang, R., Jiang, Y., Luo, D., Yu, A., and Chen, Z. (2019). Layer-based heterostructured cathodes for lithium-ion and sodium-ion batteries. Adv. Funct. Mater. *29*, 1808522.

Gao, H.C., Xin, S., Xue, L.G., and Goodenough, J.B. (2018). Stabilizing a high-energy-density rechargeable sodium battery with a solid electrolyte. Chem *4*, 833–844.

Gao, H., Cai, J., Xu, G.-L., Li, L., Ren, Y., Meng, X., Amine, K., and Chen, Z. (2019). Surface modification for suppressing interfacial parasitic reactions of a Nickel-Rich Lithium-Ion cathode. Chem. Mater. *31*, 2723–2730.

Guo, S., Liu, P., Yu, H., Zhu, Y.B., Chen, M.W., Ishida, M., and Zhou, H.S. (2015a). A layered P2- and O3-type composite as a high-energy cathode for rechargeable sodium-ion batteries. Angew. Chem. Int. Ed. *54*, 5894–5899.

Guo, S., Yu, H., Liu, P., Ren, Y., Zhang, T., Chen, M., Ishida, M., and Zhou, H.S. (2015b). High-performance symmetric sodium-ion batteries using a new, bipolar O3-type material, Na0.8Ni0.4Ti0.6O2. Energy Environ. Sci. *8*, 1237–1244.

Guo, S., Li, Q., Liu, P., Chen, M., and Zhou, H.S. (2017). Environmentally stable interface of layered oxide cathodes for sodium-ion batteries. Nat. Commun. *8*, 135.

Han, M.H., Gonzalo, E., Singh, G., and Rojo, T. (2015). A comprehensive review of sodium layered oxides: powerful cathodes for Na-ion batteries. Energy Environ. Sci. *8*, 81–102.

House, R.A., Maitra, U., Jin, L., Lozano, J.G., Somerville, J.W., Rees, N.H., Naylor, A.J., Duda, L.C., Massel, F., Chadwick, A.V., et al. (2019). What triggers oxygen loss in oxygen redox cathode materials? Chem. Mater. *31*, 3293–3300.

Hwang, J.Y., Myung, S.T., and Sun, Y.K. (2018). Quaternary transition metal oxide layered framework: O3-Type Na[$Ni_{0.32}Fe_{0.13}Co_{0.15}Mn_{0.40}$] $O_2$ cathode material for high-performance sodium-ion batteries. J. Phys. Chem. C *122*, 13500–13507.

Jung, S., and Han, Y. (2013). How do li atoms pass through the Al2O3 coating layer during lithiation in Li-ion batteries? J. Phys. Chem. Lett. *16*, 2681–2685.

Kim, I.T., Knight, J.C., Celio, H., and Manthiram, A. (2014). Enhanced electrochemical performances of Li-rich layered oxides by surface modification with reduced graphene oxide/AlPO4 hybrid coating. J. Mater. Chem. A *2*, 8696–8704.

Kong, F., Liang, C., Wang, L., Zheng, Y., Perananthan, S., Longo, R.C., Ferraris, J.P., Kim, M., and Cho, K. (2019). Kinetic stability of bulk LiNiO2 and surface degradation by oxygen evolution in LiNiO2-based cathode materials. Adv. Energy Mater. *9*, 1802586.

Lao, M., Zhang, Y., Luo, W., Yan, Q., Sun, W., and Dou, S.X. (2017). Alloy-based anode materials toward advanced sodium-ion batteries. Adv. Mater. *29*, 1700622.

Li, Y., Yang, Z., Xu, S., Mu, L., Gu, L., Hu, Y.S., Li, H., and Chen, L.Q. (2015). Air-stable copper-based P2-Na7/9Cu2/9Fe1/9Mn2/3O2 as a new positive electrode material for sodium-ion batteries. Adv. Sci. *2*, 1500031.

Li, Z.Y., Gao, R., Sun, L., Hu, Z., and Liu, X. (2017). Designing an advanced P2-$Na_{0.67}Mn_{0.65}Ni_{0.2}Co_{0.15}O_2$ layered cathode material for Na-ion batteries. J. Mater. Chem. A *3*, 16272–16278.

Liu, H., Qian, D., Verde, M.G., Zhang, M., Baggetto, L., An, K., Chen, Y., Carroll, K.J., Lau, D., Chi, M., et al. (2015). Understanding the role of NH4F and Al2O3 surface co-modification on lithium-excess layered oxide Li1.2Ni0.2Mn0.6O2. ACS Appl. Mater. Interfaces *7*, 19189–19200.

Liu, Y., Zhang, N., Wang, F., Liu, X., Jiao, L., and Fan, L.Z. (2018). Approaching the downsizing limit of maricite NaFePO4 toward high-performance cathode for sodium-ion batteries. Adv. Funct. Mater. *28*, 1801917.

Lu, Y., Zhang, Q., Li, L., Niu, Z.Q., and Chen, J. (2018a). Design strategies toward enhancing the performance of organic electrode materials in metal-ion batteries. Chem *12*, 2786–2813.

Lu, Y., Li, L., Zhang, Q., Niu, Z., and Chen, J. (2018b). Electrolyte and interface engineering for solid-state sodium batteries. Joule *2*, 1747–1770.

Luo, W.B., Chou, S.L., Zhai, Y.C., and Liu, H.K. (2014). Self-assembled graphene and LiFePO4 composites with superior high rate capability for lithium ion batteries. J. Mater. Chem. A *2*, 4927–4931.

Ma, C., Alvarado, J., Xu, J., Clément, R.-J., Kodur, M., Tong, W., Grey, C.-P., and Meng, Y.S. (2017). Exploring oxygen activity in the high energy P2-Type $Na_{0.78}Ni_{0.23}Mn_{0.69}O_2$ cathode material for Na-Ion batteries. J. Am. Chem. Soc. *139*, 4835–4845.

Palanisamy, M., Kim, H.W., Heo, S., Lee, E., and Kim, Y. (2017). Insights into the dual-electrode characteristics of layered $Na_{0.5}Ni_{0.25}Mn_{0.75}O_2$ materials for sodium-ion batteries. ACS Appl. Mater. Interfaces *9*, 10618–10625.

Park, J.S., Mane, A.U., Elam, J.W., and Croy, J.R. (2015). Amorphous Metal fluoride passivation coatings prepared by atomic layer deposition on LiCoO2 for Li-Ion Batteries. Chem. Mater. *6*, 1917–1920.

Piao, J.Y., Sun, Y.G., Duan, S.Y., Cao, A.M., Wang, X.L., Xiao, R.J., Yu, X.Q., Gong, Y., Gu, L., Li, Y., et al. (2018). Stabilizing cathode materials of lithium-ion batteries by controlling interstitial sites on the surface. Chem *7*, 1685–1695.

Piao, J.-Y., Gu, L., Wei, Z., Ma, J., Wu, J., Yang, W., Gong, Y., Sun, Y.-G., Duan, S.-Y., Tao, X.-S., et al. (2019). Phase control on surface for the stabilization of high energy cathode materials of lithium ion batteries. J. Am. Chem. Soc. *141*, 4900–4907.

Qiao, R., Dai, K., Mao, J., Weng, T.C., Sokaras, D., Nordlund, D., Song, X., Battaglia, V.S., Hussain, Z., Liu, G., and Yang, W. (2015). Revealing and suppressing surface Mn(II) formation of $Na_{0.44}MnO_2$ electrodes for Na-ion batteries. Nano Energy *16*, 186–195.

Ren, W.H., Zheng, Z., Xu, C., Niu, C.J., Wei, Q., An, Q., Zhao, K., Yan, M., Qin, M., and Mai, L.Q. (2016). Self-sacrificed synthesis of three-dimensional Na3V2(PO4)3 nanofiber network for high-rate sodium–ion full batteries. Nano Energy *25*, 145–153.

Risthaus, T., Zhou, D., Cao, X., He, X., Qiu, B., Wang, J., Zhang, L., Liu, Z., Paillard, E., Schumacher, G., et al. (2018). A high-capacity P2 $Na_{2/3}Ni_{1/3}Mn_{2/3}O_2$ cathode material for sodium ion batteries with oxygen activity. J. Power Sources *395*, 16–24.

Rong, X., Liu, J., Hu, E., Liu, Y., Wang, Y., Wu, J., Yu, X., Page, K., Hu, Y.S., Yang, W., et al. (2018). Structure-induced reversible anionic redox activity in Na layered oxide cathode. Joule *2*, 125–140.

Wang, P.F., Yao, H.R., Liu, X.Y., Zhang, J.N., Gu, L., Yu, X.Q., Xia, Y.Y., and Guo, G.Y. (2017). Ti-substituted $NaNi_{0.5}Mn_{0.5-x}Ti_xO_2$ cathodes with reversible o3−p3 phase transition for high-performance sodium-ion batteries. Adv. Mater. *29*, 1700210.

Xiao, X., Ahn, D., Liu, Z., Kim, J.H., and Lu, P. (2013). Atomic layer coating to mitigate capacity fading associated with manganese dissolution in lithium ion batteries. Electrochem. Commun. *32*, 31–34.

Xiao, Y., Wang, P.F., Xia, Y.Y., Zhu, Y.F., Yang, X.N., Zhang, X.D., Wang, Y.S., Guo, X.D., Zhong, B.H., and Guo, G.-Y. (2018). A layered–tunnel intergrowth structure for high-performance sodium-ion oxide cathode. Adv. Energy Mater. *8*, 1800492.

Yan, P., Zheng, J., Zhang, X., Xu, R., Amine, K., Xiao, J., Zhang, J.G., and Wang, C.M. (2016). Atomic to nanoscale investigation of functionalities of an $Al_2O_3$ coating layer on a cathode for enhanced battery performance. Chem. Mater. *28*, 857–863.

Yang, H., Piper, D.M., Gu, M., Travis, J.J., George, S.M., Lee, S.H., Genc, A., Pullan, L., Liu, J., Mao, S.X., et al. (2014). In situ transmission electron microscopy probing of native oxide and artificial layers on silicon nanoparticles for lithium ion batteries. ACS Nano *11*, 11816–11823.

Yao, H.-R., Wang, P.F., Wang, Y., Yu, X.-Q., Xia, Y.Y., and Guo, G.-Y. (2017). Excellent comprehensive performance of Na-based layered oxide benefiting from the synergetic contributions of multimetal ions. Adv. Energy Mater. *2017*, 1700189.

Yin, Y., Xiong, F., Pei, C., Xu, Y., Qin, Q., Tan, S., Zhuang, Z., Sheng, J., Li, Q., and Mai, L.Q. (2017). Robust three-dimensional graphene skeleton encapsulated Na3V2O2(PO4)2F nanoparticles as a high-rate and long-life cathode of sodium-ion batteries. Nano Energy *41*, 452–459.

Yuan, S., Zhu, Y., Li, W., Wang, S., Xu, D., Li, L., Zhang, Y., and Zhang, X.B. (2017). Surfactant-free

aqueous synthesis of pure single-crystalline SnSe nanosheet clusters as anode for high energy- and power-density sodium-ion batteries. Adv. Mater. *29*, 1602469.

Zhan, C., Lu, J., Kropf, A.J., Wu, T., Jansen, A.N., Sun, Y.K., Qiu, X., and Amine, K. (2013). Mn(II) deposition on anodes and its effects on capacity fade in spinel lithium manganate–carbon systems. Nat. Commun. *4*, 2437.

Zhan, C., Wu, T., Lu, J., and Amine, K. (2018). Dissolution, migration, and deposition of transition metal ions in Li-ion batteries exemplified by Mn-based cathodes – a critical review. Energy Environ. Sci. *11*, 243–257.

Zhang, X.H., Pang, W.L., Wan, F., Guo, J.Z., Lü, H.-Y., Li, J.Y., Xing, Y.M., Zhang, J.P., and Wu, X.L. (2016a). P2–Na2/3Ni1/3Mn5/9Al1/9O2 microparticles as superior cathode material for sodium-ion batteries: enhanced properties and mechanism via graphene connection. ACS Appl. Mater. Interfaces *8*, 20650–20659.

Zhang, Y., Zhao, H., and Du, Y. (2016b). Symmetric full cells assembled by using self-supporting Na3V2(PO4)3 bipolar electrodes for superior sodium energy storage. J. Mater. Chem. A *4*, 7155–7159.

Zhu, T., Hu, P., Wang, X.P., Liu, Z.H., Luo, W., Owusu, K.A., Cao, W.W., Shi, C.W., Li, J.T., Zhou, L., and Mai, L.Q. (2019). Realizing three-electron redox reactions in NASICON-structured $Na_3MnTi(PO_4)_3$ for sodium-ion batteries. Adv. Energy Mater. *9*, 1803436.

**ISCI, Volume *19***

## Supplemental Information

# Surface Stabilization of O3-type Layered Oxide Cathode to Protect the Anode of Sodium Ion Batteries for Superior Lifespan

**Qi Zhang, Qin-Fen Gu, Yang Li, Hai-Ning Fan, Wen-Bin Luo, Hua- Kun Liu, and Shi-Xue Dou**

**Supplemental Information**

# Surface Stabilization of O3-Type Layered Oxide Cathode to Protect the Anode of Sodium ion Batteries for Superior Lifespan

Qi Zhang; Qin-Feng Gu*; Yang Li; Hai-Ning Fan; Wen-Bin Luo*; Hua- Kun Liu; Shi-Xue Dou

## Transparent methods

### Synthetic procedures and characterization

#### Preparation of cathode materials P-NMNM and C-NMNM

$Na[Li_{0.05}Mn_{0.50}Ni_{0.30}Cu_{0.10}Mg_{0.05}]O_2$ was synthesized as in our previous report.[6] It was the dispersed into pure ethanol to form solution A. Certain amounts of $Al(NO_3)_3 \cdot 9H_2O$ were dispersed in solution A under vigorous stirring. A given mass of $H_3PO_4$ was added dropwise to the above solution under vigorous stirring for 2 h. The resulting mixture was purified in a rotary evaporator and calcined at 400 $^oC$.

#### Material characterization

XRD measurements were performed to investigate the crystal structure using a PLXcel 3D X-ray diffractometer with a non-monochromated Cu Kα X-ray source. The morphology of the samples was examined using field emission scanning electron microscopy (FE-SEM; JEOL JSM-7500). STEM, EELS, and EDS were performed using a 200 kV JEOL 2011 instrument. Synchrotron powder diffraction data were collected at the Australian Synchrotron beamline with a wavelength (λ) of 0.688 Å, calibrated with the standard reference material (National Institute of Standards and

Technology (NIST) LaB6 660b). Schematic representations of the data were obtained by VESTA software.

**Electrochemical characterization**

The electrochemical properties were evaluated by using R2032-type coin cells assembled in an argon-filled glove box. Positive electrodes were prepared by mixing 80 wt. % active materials, 10 wt. % acetylene black, and 10 wt. % polyvinylidene fluoride (PVDF) in N-methyl-2-pyrrolidone and coating the slurry on Al foil. The electrodes were dried at 120 °C in vacuum. The mass loading of the electrodes was in the range of 3.0 – 4.5 mg $cm^{-2}$. Hard carbon electrodes were obtained with 90 % hard carbon, 5 % acetylene black, and 5 % carboxymethyl cellulose (CMC). The electrolyte was 1 M NaClO4 dissolved in ethylene carbonate/diethyl carbonate (EC/ DEC, 1:1 by volume) with 5 vol. % fluoroethylene carbonate as an electrolyte additive. Na metal and hard carbon electrodes were the negative electrodes for the half cell and full cell, respectively. In the case of the full cell, the current density is based on the mass of cathode material. The weight ratio of the two electrodes was balanced with reference to their corresponding reversible capacities. The full cell system was activated by operating it at 0.1 C in the voltage window of 1.0 – 4.19 V.6 In the following test, the voltage window was 1.0 – 4.0 V. A Celgard 2400 membrane was used as the separator. Galvanostatic charge/discharge tests were performed on a LAND multichannel battery testing system (CT2001A, Wuhan Jinnuo Electronics Co., Ltd.). CV curves were acquired with an electrochemical workstation (Bio-logic EC Lab VMP3).

**Supplemental Figures**

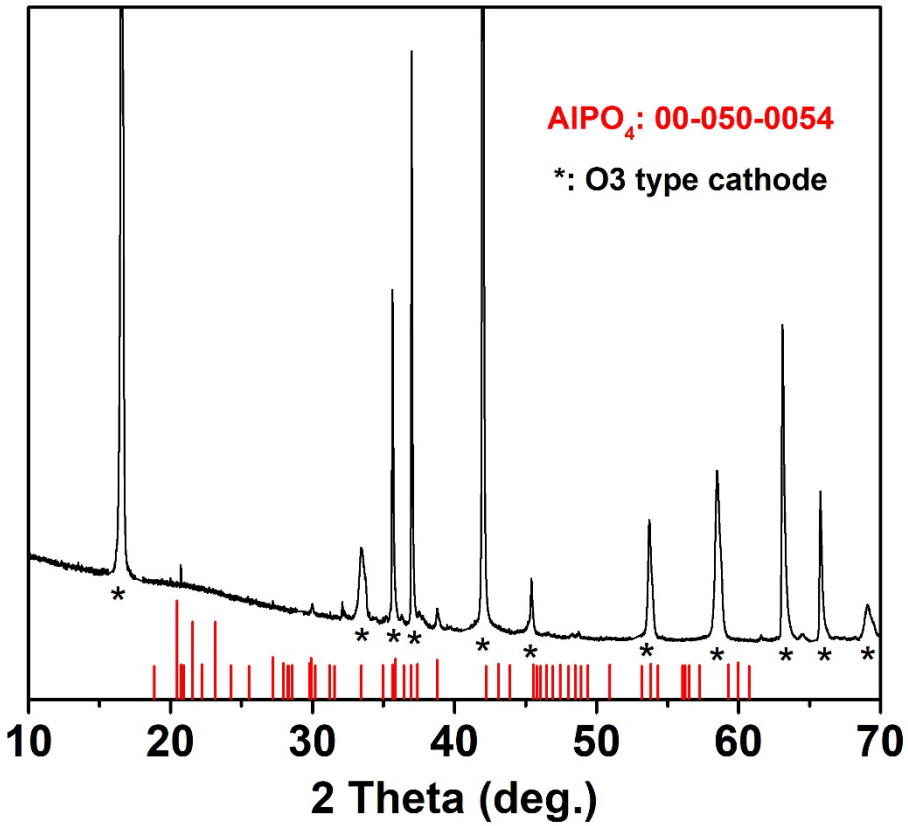


**Figure S1. PXRD patterns of C-NMNM, Related to Figures 1**

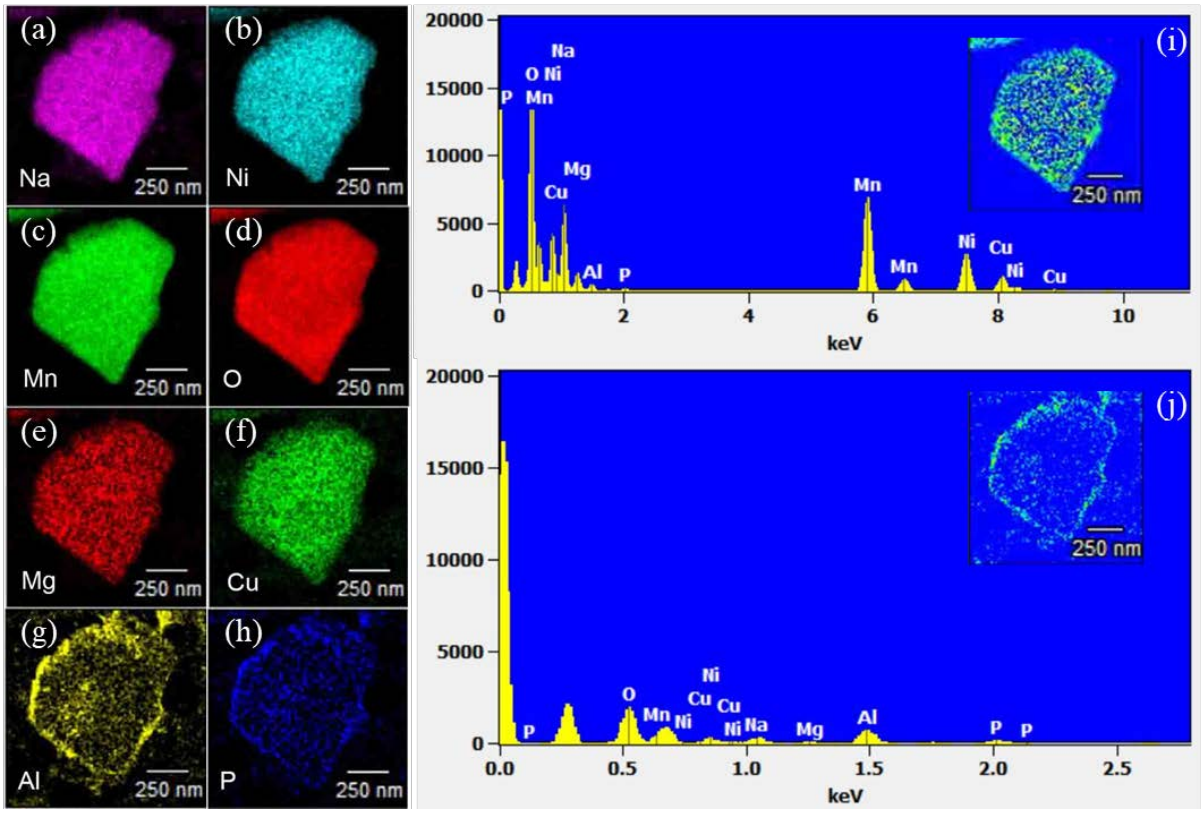


**Figure S2. (a-h) Different element distributions from HAADF-STEM-EDS mapping; (i, j) phase distributions (insets) and EDS spectra of core (top) and shell (bottom) of C-NMNM, Related to Figures 1**

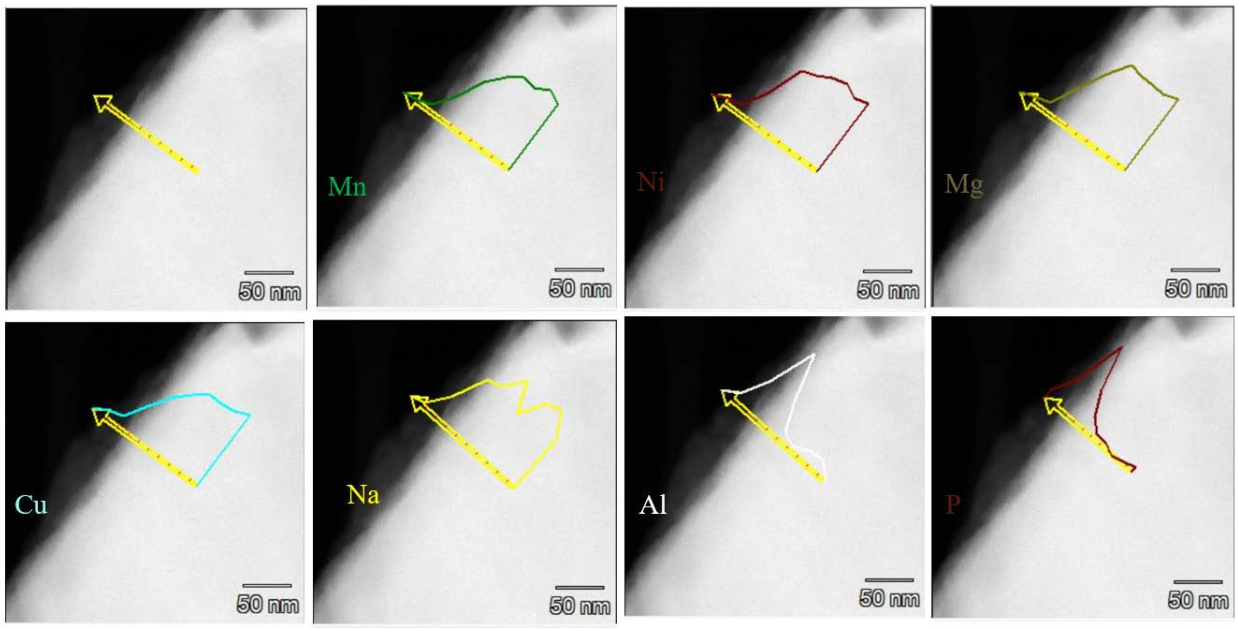


**Figure S3. Different element distributions in the edge area, Related to Figures 1**

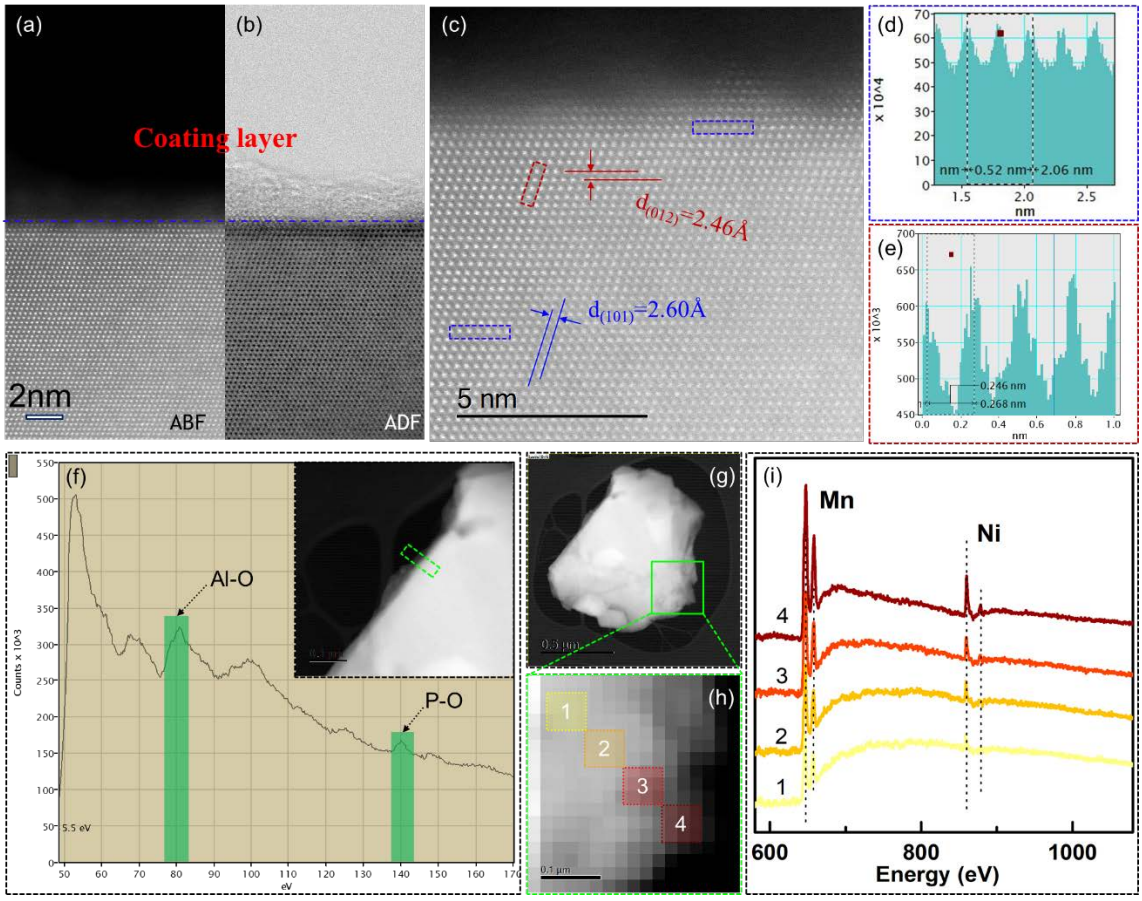


**Figure S4. Composition, structure, and crystalline phase of the C-NMNM samples. (a, b) HAADF and annular bright field (ABF)-STEM images show the interface of the coating layer in the same local region. (c) HAADF-STEM image shows the crystal structure of the cathode material after modification; (d, e) Intensity profiles of each bright line in (c). (f) EELS image of the outer layer of the particle, with selected area as inset image; (g, h) HAADF-STEM images with regions indicated for the corresponding EELS data shown in (i), Related to Figures 1**

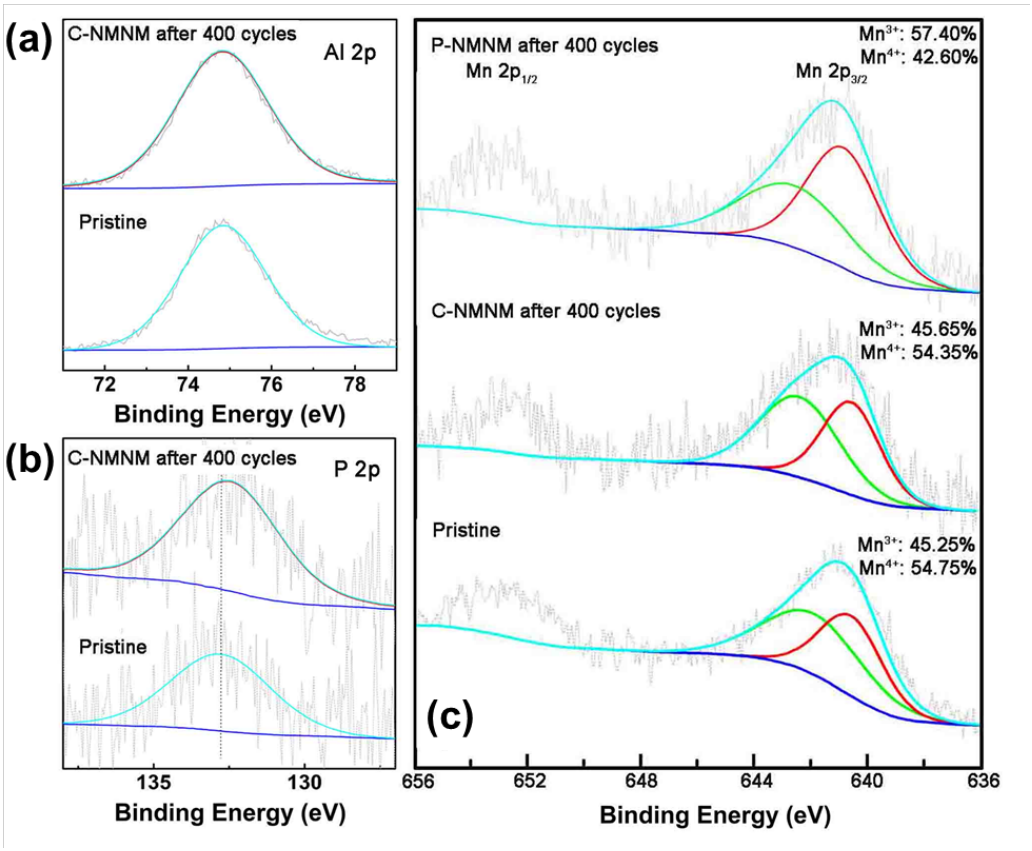


**Figure S5. XPS results for before and after coating: Al 2p (a), P 2p (b), and Mn 2p (c), Related to Figures 1**

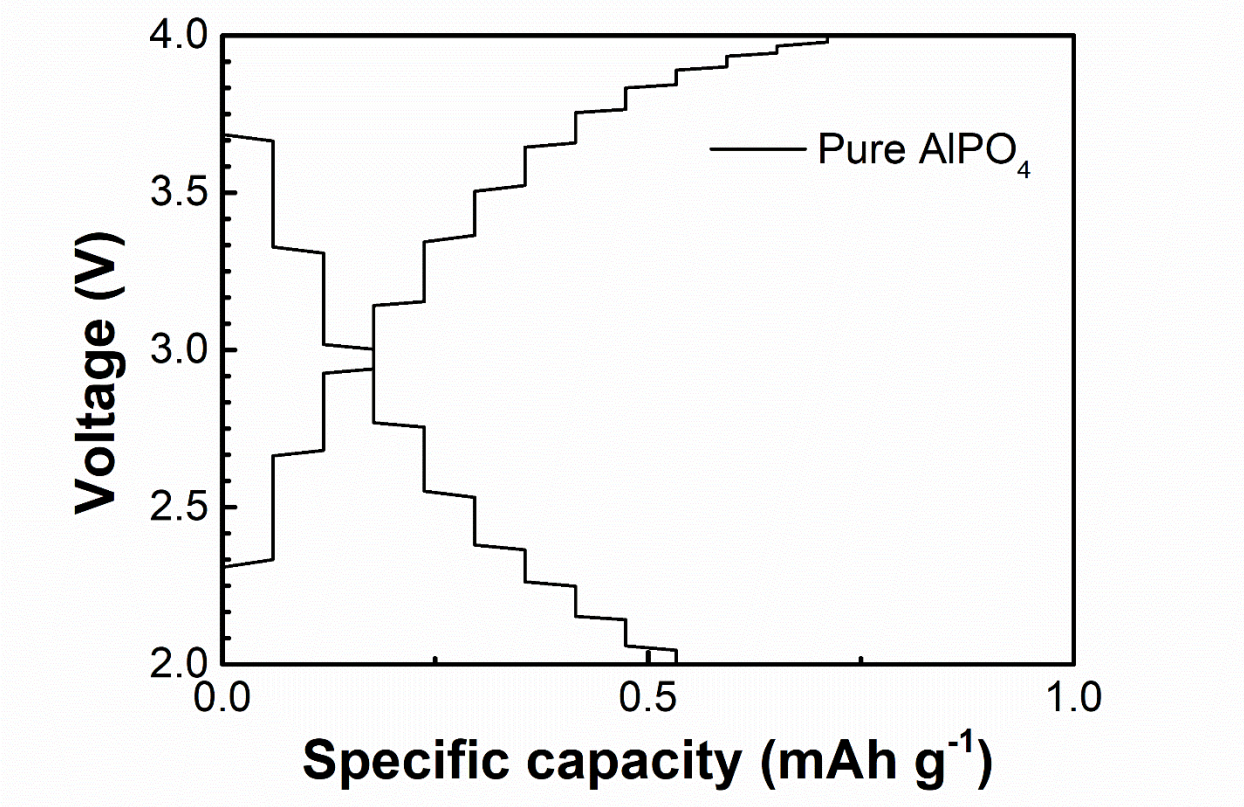


**Figure S6. The charge and discharge profiles of pure $AlPO_4$, Related to Figures 2**

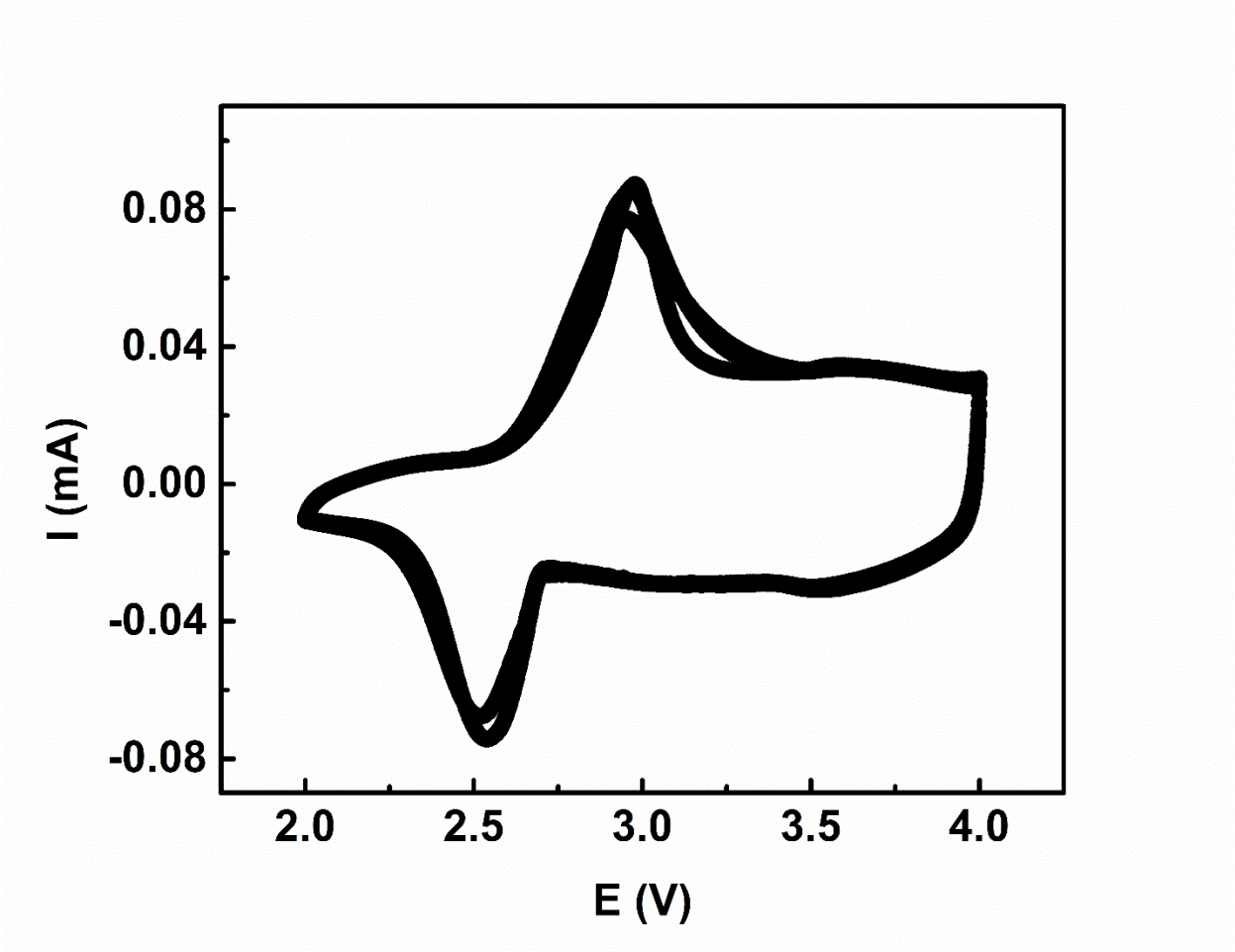


**Figure S7. Cyclic voltammetry (CV) curves of C-NMNM electrode, Related to Figures 2**

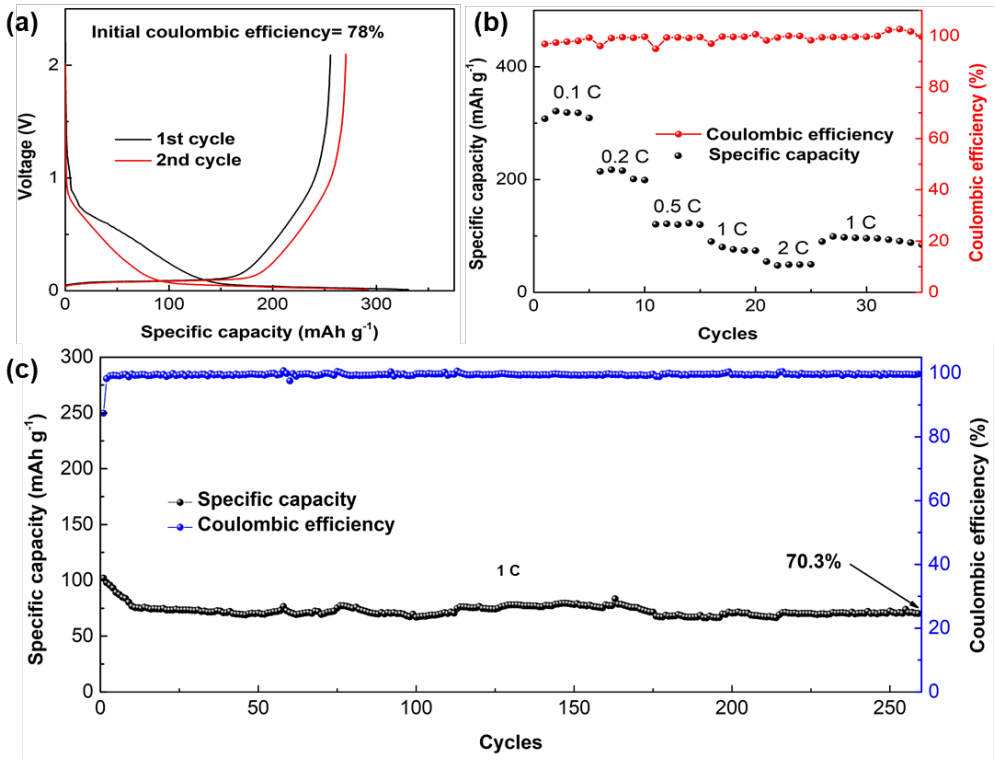


**Figure S8. The electrochemical performance of Hard carbon. (a) The initial two cycles of charge and discharge. (b) Rate performance. (c) cycle performance at 1C, Related to Figures 3**

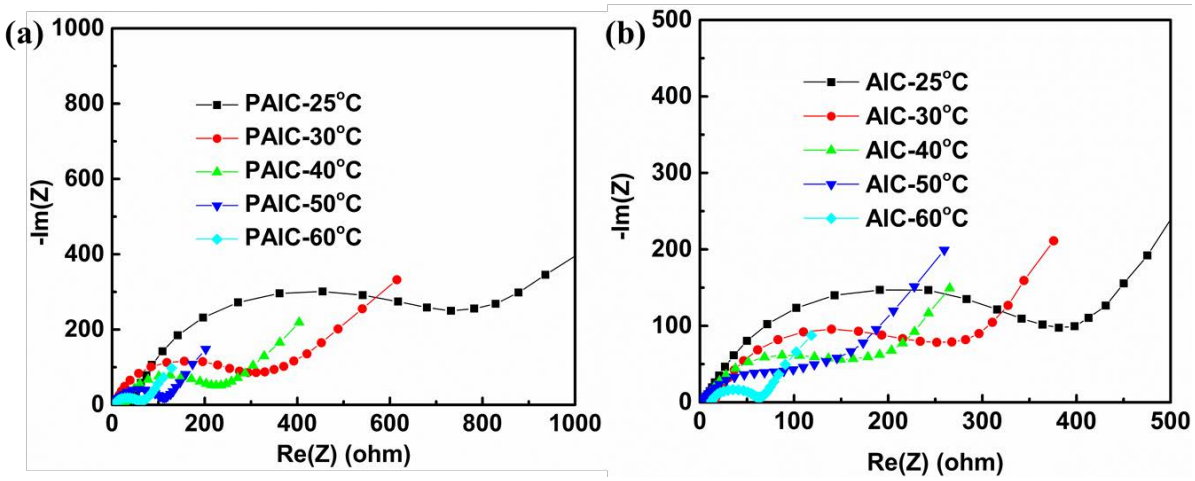


**Figure S9. The electrochemical impedance spectra of P-NMNM and C-NMNM electrodes in half cells at different temperatures: (a) P-NMNM and (b) C-NMNM, Related to Figures 3**

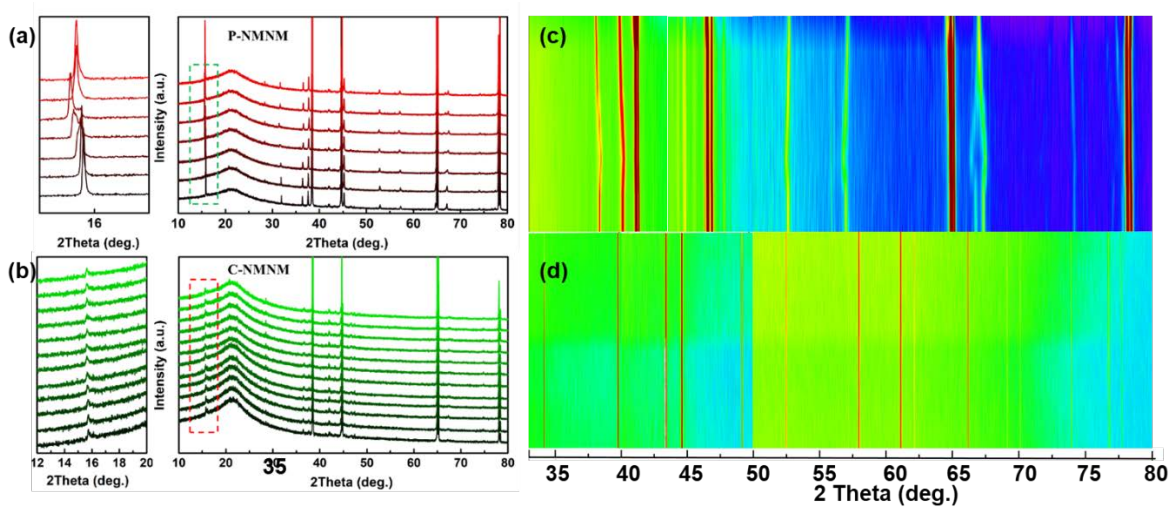


**Figure S10. In Situ PXRD Characterization for P-NMNM (a) and C-NMNM(b) electrode during the Charge and Discharge Process. (c, d) The corresponding contour plot of a, b, Related to Figures 4**

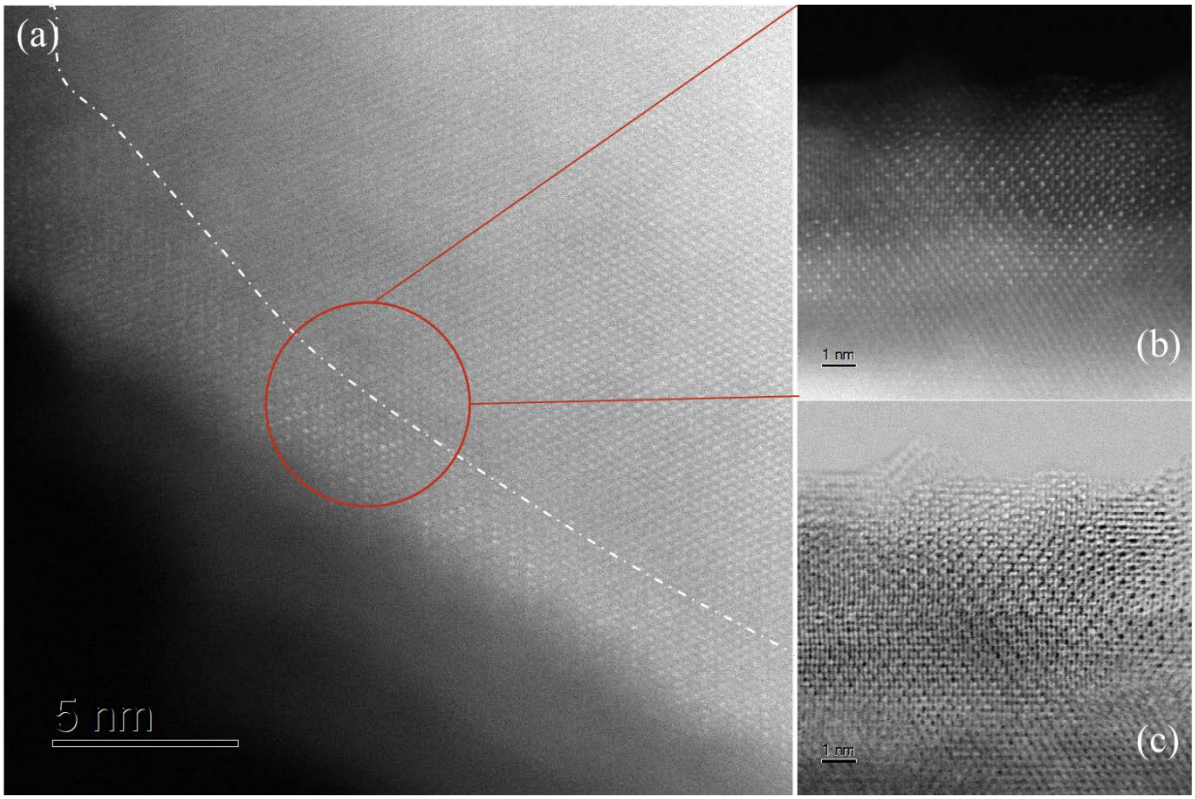


**Figure S11**. **Detailed HAADF-STEM information on P-NMNM after 200 cycles, showing the interface between the different phases (a), P-NMNM (b) and spinel phase with Na occupying the tetrahedral sites (c), Related to Figures 4**

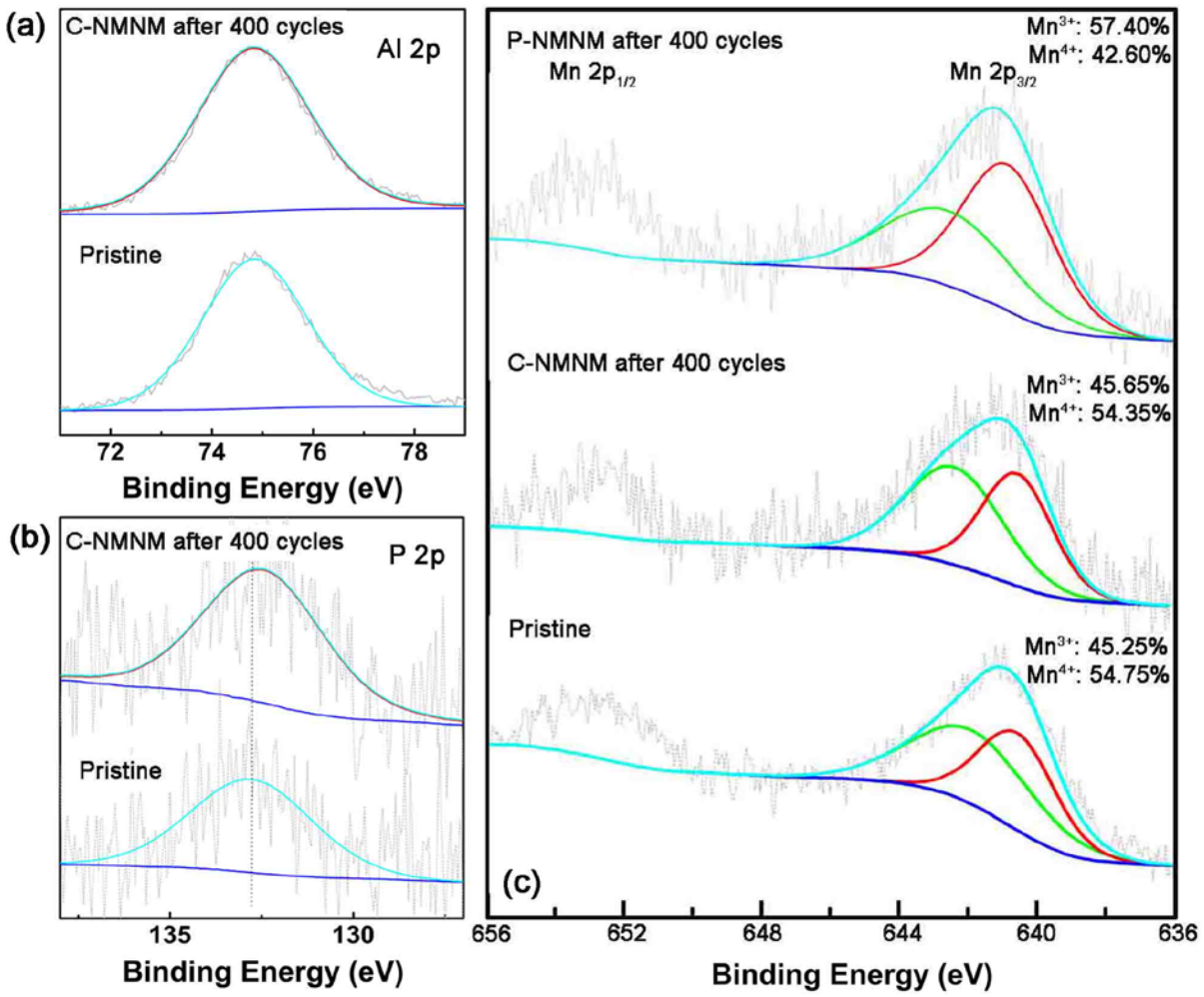


**Figure S12. Valence states of the C-NMNM before and after 400 cycles. XPS spectra of Al 2p (a), P 2p (b), and Mn 2p (c), Related to Figures 5**

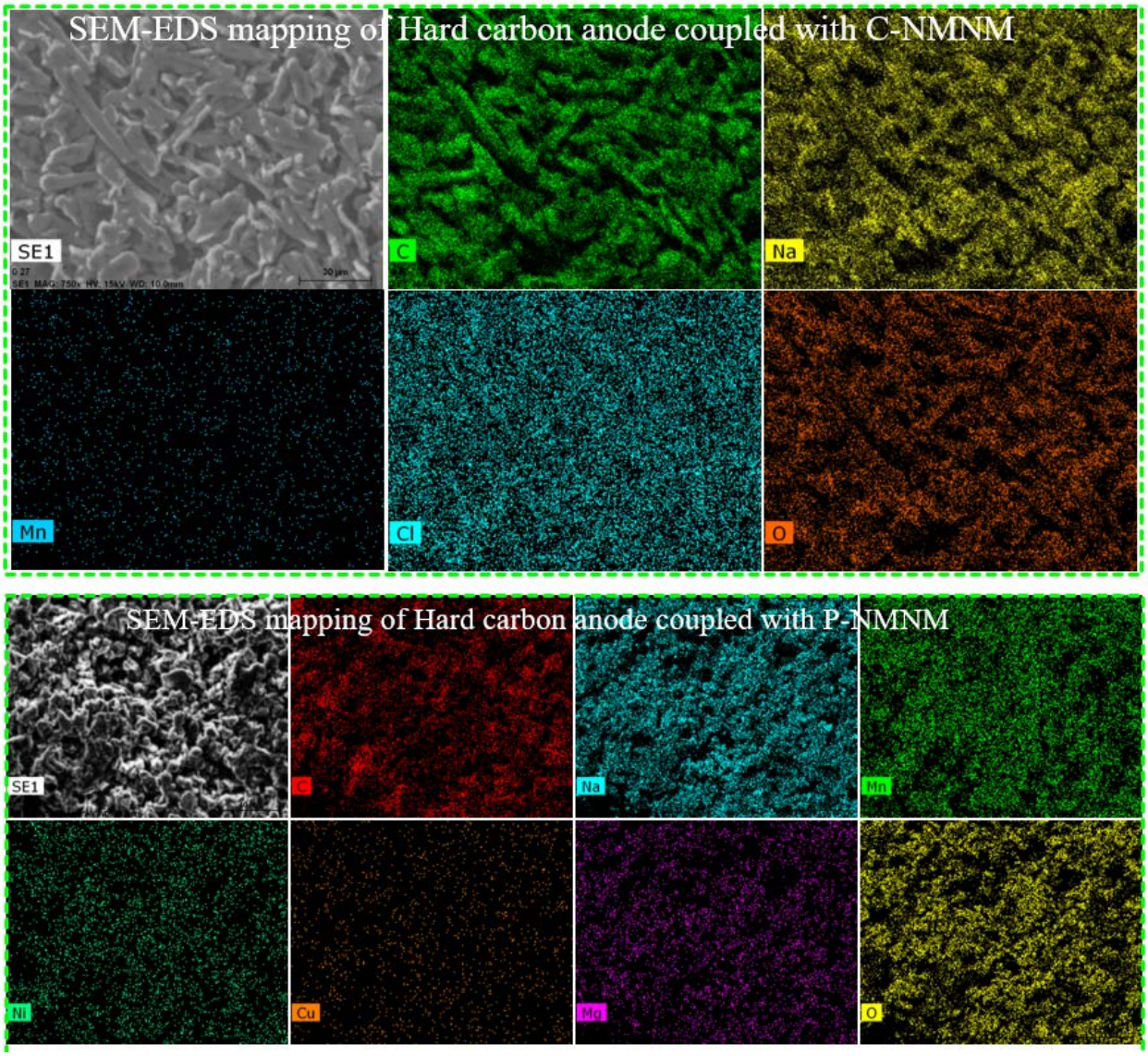


**Figure S13. SEM-EDS mapping of hard carbon anode coupled with C-NMNM and P-NMNM, respectively, Related to Figures 5**

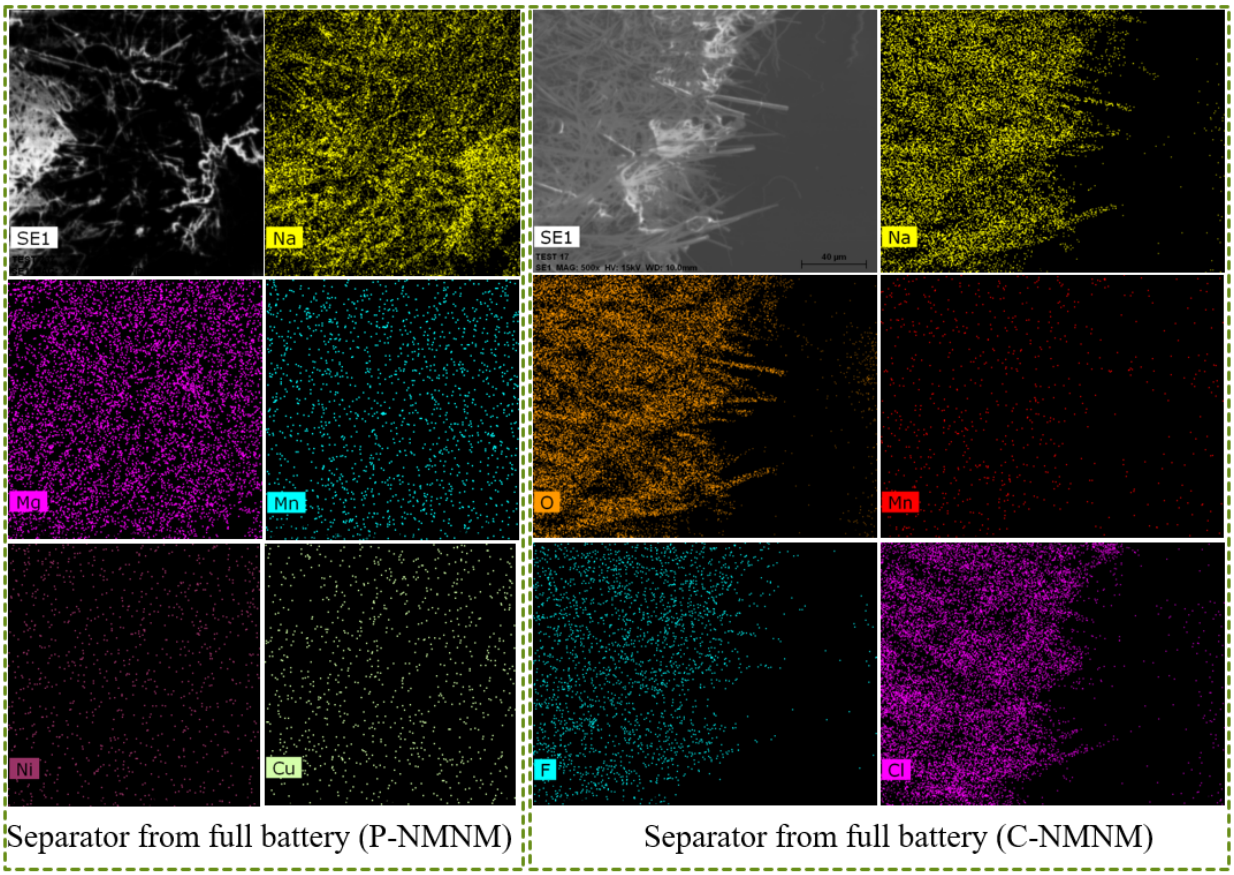


**Figure S14. SEM-EDS mapping of separator coupled with C-NMNM and P-NMNM, respectively, Related to Figures 5**

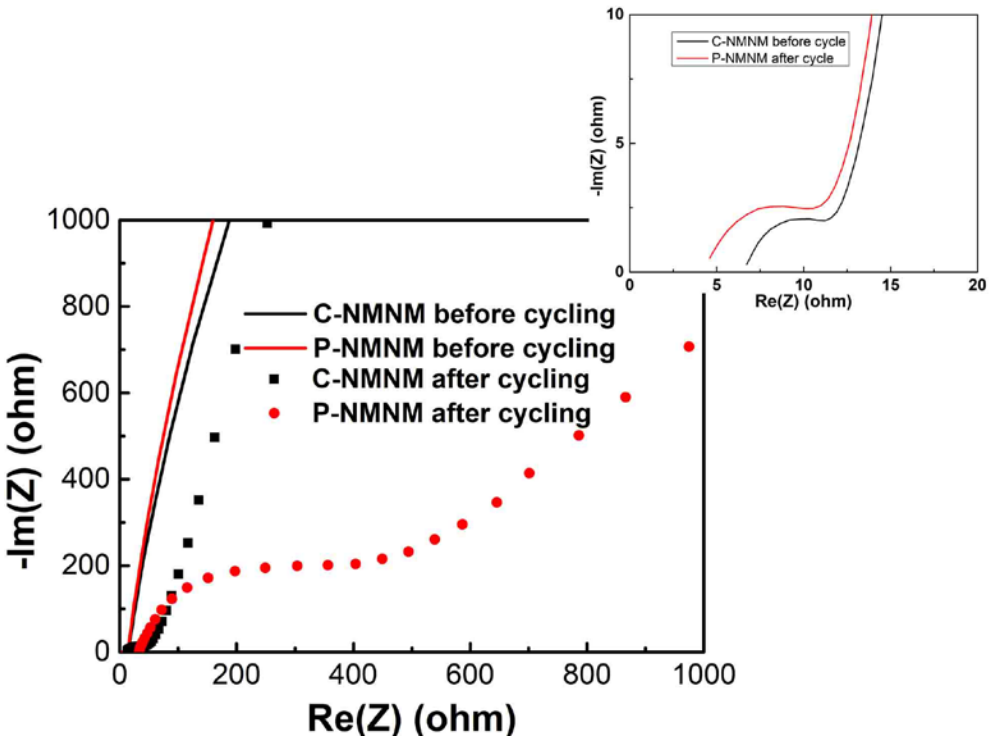


**Figure S15. EIS plots of P-NMNM and C-NMNM before and after 200 cycles in full battery system, with the inset showing an enlargement of the indicated range, Related to Figures 5**